



## Calhoun: The NPS Institutional Archive

---

Theses and Dissertations

Thesis Collection

---

2006-06

# Characterization and analysis of a multicolor quantum well infrared photodetector

Hanson, Nathan A.

Monterey, California. Naval Postgraduate School

---

<http://hdl.handle.net/10945/2842>



Calhoun is a project of the Dudley Knox Library at NPS, furthering the precepts and goals of open government and government transparency. All information contained herein has been approved for release by the NPS Public Affairs Officer.

**Dudley Knox Library / Naval Postgraduate School**  
**411 Dyer Road / 1 University Circle**  
**Monterey, California USA 93943**

<http://www.nps.edu/library>



# **NAVAL POSTGRADUATE SCHOOL**

**MONTEREY, CALIFORNIA**

## **THESIS**

**CHARACTERIZATION AND ANALYSIS OF A  
MULTICOLOR QUANTUM WELL INFRARED  
PHOTODETECTOR**

by

Nathan A. Hanson

June 2006

Thesis Advisor:  
Co-Advisor:

Gamani Karunasiri  
James H. Luscombe

**Approved for public release; distribution is unlimited**

THIS PAGE INTENTIONALLY LEFT BLANK

<b>REPORT DOCUMENTATION PAGE</b>			<i>Form Approved OMB No. 0704-0188</i>	
Public reporting burden for this collection of information is estimated to average 1 hour per response, including the time for reviewing instruction, searching existing data sources, gathering and maintaining the data needed, and completing and reviewing the collection of information. Send comments regarding this burden estimate or any other aspect of this collection of information, including suggestions for reducing this burden, to Washington headquarters Services, Directorate for Information Operations and Reports, 1215 Jefferson Davis Highway, Suite 1204, Arlington, VA 22202-4302, and to the Office of Management and Budget, Paperwork Reduction Project (0704-0188) Washington DC 20503.				
<b>1. AGENCY USE ONLY (Leave blank)</b>		<b>2. REPORT DATE</b> June 2006	<b>3. REPORT TYPE AND DATES COVERED</b> Master's Thesis	
<b>4. TITLE AND SUBTITLE:</b> Characterization and Analysis of a Multicolor Quantum Well Infrared Photodetector			<b>5. FUNDING NUMBERS</b>	
<b>6. AUTHOR(S)</b> Nathan A. Hanson				
<b>7. PERFORMING ORGANIZATION NAME(S) AND ADDRESS(ES)</b> Naval Postgraduate School Monterey, CA 93943-5000			<b>8. PERFORMING ORGANIZATION REPORT NUMBER</b>	
<b>9. SPONSORING /MONITORING AGENCY NAME(S) AND ADDRESS(ES)</b> N/A			<b>10. SPONSORING/MONITORING AGENCY REPORT NUMBER</b>	
<b>11. SUPPLEMENTARY NOTES</b> The views expressed in this thesis are those of the author and do not reflect the official policy or position of the Department of Defense or the U.S. Government.				
<b>12a. DISTRIBUTION / AVAILABILITY STATEMENT</b> Approved for public release; distribution unlimited			<b>12b. DISTRIBUTION CODE</b>	
<b>13. ABSTRACT (maximum 200 words)</b> <p>This thesis presents analysis and characterization of performance of a newly designed, multicolor quantum well infrared photodetector (QWIP). Specifically, it focuses on a detector capable of detecting infrared emissions in the near infrared (NIR), mid-wavelength infrared (MWIR), and long-wavelength infrared (LWIR). Through photocurrent spectroscopy and performance analysis, this prototype detector can be classified and prepared for possible future use within the U.S. Armed Forces. Certain military applications require a highly accurate, reliable, sensitive, and multispectral infrared detector to identify targets and ensure mission success. By designing and fabricating a multicolor quantum well infrared photodetector, simultaneous detection of targets in the near infrared, mid-wavelength infrared and long-wavelength infrared is possible using only one detector. In addition, power and cooling requirements for quantum well infrared detectors makes them suitable for use in the field.</p>				
<b>14. SUBJECT TERMS</b> Quantum Well, QWIP, Three-color detection, Infrared detection, Photocurrent Measurement, I-V Curve Measurement.			<b>15. NUMBER OF PAGES</b> 67	
			<b>16. PRICE CODE</b>	
<b>17. SECURITY CLASSIFICATION OF REPORT</b> Unclassified	<b>18. SECURITY CLASSIFICATION OF THIS PAGE</b> Unclassified	<b>19. SECURITY CLASSIFICATION OF ABSTRACT</b> Unclassified	<b>20. LIMITATION OF ABSTRACT</b> UL	

THIS PAGE INTENTIONALLY LEFT BLANK

**Approved for public release; distribution is unlimited.**

**CHARACTERIZATION AND ANALYSIS OF A MULTICOLOR QUANTUM  
WELL INFRARED PHOTODETECTOR**

Nathan A. Hanson  
Ensign, United States Navy  
B.S., Jacksonville University, 2005

Submitted in partial fulfillment of the  
requirements for the degree of

**MASTER OF SCIENCE IN APPLIED PHYSICS**

from the

**NAVAL POSTGRADUATE SCHOOL  
June 2006**

Author: Nathan A. Hanson

Approved by: Gamani Karunasiri  
Thesis Advisor

James H. Luscombe  
Co-Advisor

James H. Luscombe  
Chairman, Department of Physics

THIS PAGE INTENTIONALLY LEFT BLANK

## **ABSTRACT**

This thesis presents analysis and characterization of performance of a newly designed, multicolor quantum well infrared photodetector (QWIP). Specifically, it focuses on a detector capable of detecting infrared emissions in the near infrared (NIR), mid-wavelength infrared (MWIR), and long-wavelength infrared (LWIR). Through photocurrent spectroscopy and performance analysis, this prototype detector can be classified and prepared for possible future use within the U.S. Armed Forces. Certain military applications require a highly accurate, reliable, sensitive, and multispectral infrared detector to identify targets and ensure mission success. By designing and fabricating a multicolor quantum well infrared photodetector, simultaneous detection of targets in the near infrared, mid-wavelength infrared and long-wavelength infrared is possible using only one detector. In addition, power and cooling requirements for quantum well infrared detectors makes them suitable for use in the field.



THIS PAGE INTENTIONALLY LEFT BLANK

# TABLE OF CONTENTS

<b>I.</b>	<b>INTRODUCTION.....</b>	<b>1</b>
<b>A.</b>	<b>INFRARED DETECTION .....</b>	<b>1</b>
<b>B.</b>	<b>THE QUANTUM WELL .....</b>	<b>5</b>
<b>C.</b>	<b>MULTICOLOR INFRARED PHOTODETECTOR .....</b>	<b>11</b>
<b>II.</b>	<b>I-V CHARACTERISTICS.....</b>	<b>17</b>
<b>A.</b>	<b>I-V MEASUREMENT.....</b>	<b>17</b>
<b>B.</b>	<b>EXPERIMENTAL RESULTS.....</b>	<b>18</b>
1.	Near Infrared Detector .....	18
2.	Mid-Wavelength Infrared Detector .....	20
3.	Long-Wavelength Infrared Detector.....	22
<b>III.</b>	<b>PHOTOCURRENT MEASUREMENT .....</b>	<b>25</b>
<b>A.</b>	<b>INTRODUCTION.....</b>	<b>25</b>
1.	Experimental Setup .....	25
2.	Converting Photocurrent to an Electrical Signal.....	27
3.	Calculating and Interpreting Responsivity .....	28
<b>B.</b>	<b>BIAS DEPENDANCE OF RESPONSIVITY .....</b>	<b>29</b>
1.	Near Infrared Detector .....	29
2.	Mid-Wavelength Infrared Detector .....	31
3.	Long-Wavelength Infrared Detector.....	33
<b>C.</b>	<b>TEMPERATURE DEPENDENCE.....</b>	<b>35</b>
1.	Near Infrared Detector .....	36
2.	Mid-Wavelength Infrared Detector .....	38
3.	Long-Wavelength Infrared Detector.....	40
<b>IV.</b>	<b>CONCLUSION .....</b>	<b>43</b>
<b>A.</b>	<b>OVERALL DETECTOR RELIABILITY .....</b>	<b>43</b>
<b>B.</b>	<b>MILITARY APPLICATIONS .....</b>	<b>45</b>
<b>C.</b>	<b>RECOMMENDATIONS AND FUTURE WORK .....</b>	<b>45</b>
<b>APPENDIX A: AGILENT 4155B SEMICONDUCTOR PARAMETER ANALYZER OPERATION.....</b>		<b>47</b>
<b>LIST OF REFERENCES.....</b>		<b>49</b>
<b>INITIAL DISTRIBUTION LIST .....</b>		<b>51</b>

THIS PAGE INTENTIONALLY LEFT BLANK

## LIST OF FIGURES

Figure 1.	Transmittance of air and absorbing molecules by wavelength (From Ref. [1]).....	2
Figure 2.	Creation of electron-hole pair by (a) direct and (b) indirect transition as a result of photon absorption (After Ref. [8]).....	4
Figure 3.	Intrinsic and extrinsic transitions with respect to a vertical energy profile (From Ref. [8]).....	4
Figure 4.	Example of quantized energy levels in a GaAs/AlGaAs quantum well (From Ref. [8]).....	6
Figure 5.	Discrete energy levels in a symmetric quantum well (From Ref. [1]).....	7
Figure 6.	Example of an asymmetric well with allowable intersubband transitions (From Ref. [15]).....	9
Figure 7.	Incident angle of applied radiation for intersubband measurement as required by the polarization selection rule (From Ref. [8]).....	9
Figure 8.	Effects of positive and negative biasing on symmetric and asymmetric wells (From Ref. [1]).....	10
Figure 9.	Physical structure of the multicolor detection device (From Ref. [1]).....	11
Figure 10.	Structural diagram of device with angled incident radiation and external contacts applied (From Ref. [1]).....	12
Figure 11.	Potential profile for all three quantum well stacks (From Ref. [1]).....	12
Figure 12.	NIR detector potential profile and layer description (From Ref. [1]).....	13
Figure 13.	MWIR detector potential profile and layer description (From Ref. [1]).....	14
Figure 14.	LWIR detector potential profile and layer description (From Ref. [1]).....	14
Figure 15.	Plot of energy bandgap vs. lattice constants for major III-V compounds (After Ref. [14]).....	15
Figure 16.	NIR detector I-V curves with cold aluminum shield. The dashed red curve corresponds to I-V without the shield at 10 K. ....	19
Figure 17.	NIR detector I-V curves without the aluminum shield.....	19
Figure 18.	MWIR detector I-V curves with cold aluminum shield. The dashed red curve corresponds to I-V without the shield at 10 K. ....	21
Figure 19.	MWIR detector I-V curves without the aluminum shield in place.....	21
Figure 20.	LWIR detector I-V curves with cold aluminum shield. The dashed red curve corresponds to I-V without the shield at 10 K. ....	22
Figure 21.	LWIR detector I-V curves without the aluminum shield.....	23
Figure 22.	Photograph of photodetector characterization system setup.....	26
Figure 23.	Mirror and beam splitter assembly with reference (bottom left) and cooled (top right) detectors shown. ....	26
Figure 24.	External bias junction box. ....	27
Figure 25.	Lock-in amplifiers for photocurrent and reference voltage measurement.....	27
Figure 26.	Responsivity as a function of wavelength of the NIR detector for a set of forward bias voltages using the visible light source. ....	30

Figure 27.	Responsivity as a function of wavelength of the NIR detector for a set of reverse bias voltages using the visible light source. ....	31
Figure 28.	Responsivity as a function of wavelength for the MWIR detector for a set of forward bias voltages. ....	32
Figure 29.	Responsivity as a function of wavelength for the MWIR detector for a set of reverse bias voltages. ....	33
Figure 30.	Responsivity as a function of wavelength for the LWIR detector for a set of forward bias voltages. ....	34
Figure 31.	Responsivity as a function of wavelength for the LWIR detector for a set of reverse bias voltages. ....	35
Figure 32.	Responsivity as a function of temperature for the NIR detector with a constant 2 V forward bias applied. ....	36
Figure 33.	Responsivity as a function of temperature for the NIR detector with a constant -2 V reverse bias applied. ....	37
Figure 34.	NIR peak responsivity vs. temperature at 0.845 $\mu\text{m}$ and 0.935 $\mu\text{m}$ peaks. ....	38
Figure 35.	Responsivity as a function of temperature for the MWIR detector with a constant 3.5 V forward bias applied. ....	39
Figure 36.	Responsivity as a function of temperature for the MWIR detector with a constant -3.5 V reverse bias applied. ....	40
Figure 37.	Responsivity as a function of temperature for the LWIR detector with a constant 1 V forward bias applied. ....	41
Figure 38.	Responsivity as a function of temperature for the LWIR detector with a constant -1 V reverse bias applied. ....	42

## LIST OF TABLES

Table 1.	Description of QWIP composition by layer (From Ref. [9]).	13
----------	---	----

THIS PAGE INTENTIONALLY LEFT BLANK

## **ACKNOWLEDGMENTS**

I would like to express my gratitude to Professor Gamani Karunasiri for his guidance and expertise throughout this project. I would also like to thank Fabio Durante P. Alves, without whom this project would have never gotten started. Lastly, I would like to extend thanks to my wife, Jaymi, for her love, support, and patience through this graduate school process.



THIS PAGE INTENTIONALLY LEFT BLANK

# **I. INTRODUCTION**

The purpose of this thesis is to analyze and characterize the performance of a newly designed multicolor infrared photodetector using quantum well technology. This device was designed and sent for fabrication by Fabio Durante P. Alves as part of an ongoing investigation, by the Sensors Research Lab at the Naval Postgraduate School, into the usability of quantum well infrared photodetectors (QWIP's) for military applications. Specifically, this thesis will focus on a detector capable of detecting infrared emissions in the near infrared (NIR), mid-wavelength infrared (MWIR), and long-wavelength infrared (LWIR) within a single device.

## **A. INFRARED DETECTION**

Infrared radiation is a form of electromagnetic radiation with wavelengths ranging from just under one micrometer to about one millimeter in length. This region is further subdivided into the near infrared (0.7-3  $\mu\text{m}$ ), mid-wavelength infrared (3-6  $\mu\text{m}$ ), long-wavelength infrared (6-15  $\mu\text{m}$ ), and Terahertz ( $10^{12}$  Hertz) regions. Within these regions, atmospheric absorption due to water,  $\text{CO}_2$ , and other airborne molecules limit the ranges that we can effectively detect incoming photon radiation. In order to reduce this effect, infrared detectors are optimally designed within ranges where transmittance is the greatest. For the purpose of this thesis, we will focus on the first three sub regions and disregard the Terahertz region. The atmospheric transmittance, shown in Figure 1, limits our possible detection ranges to 0.7-2.5  $\mu\text{m}$ , 3-5  $\mu\text{m}$ , and 8-14  $\mu\text{m}$  corresponding to the near, middle and far infrared ranges respectively. It is within these narrow ranges that the design of this detector has been focused.

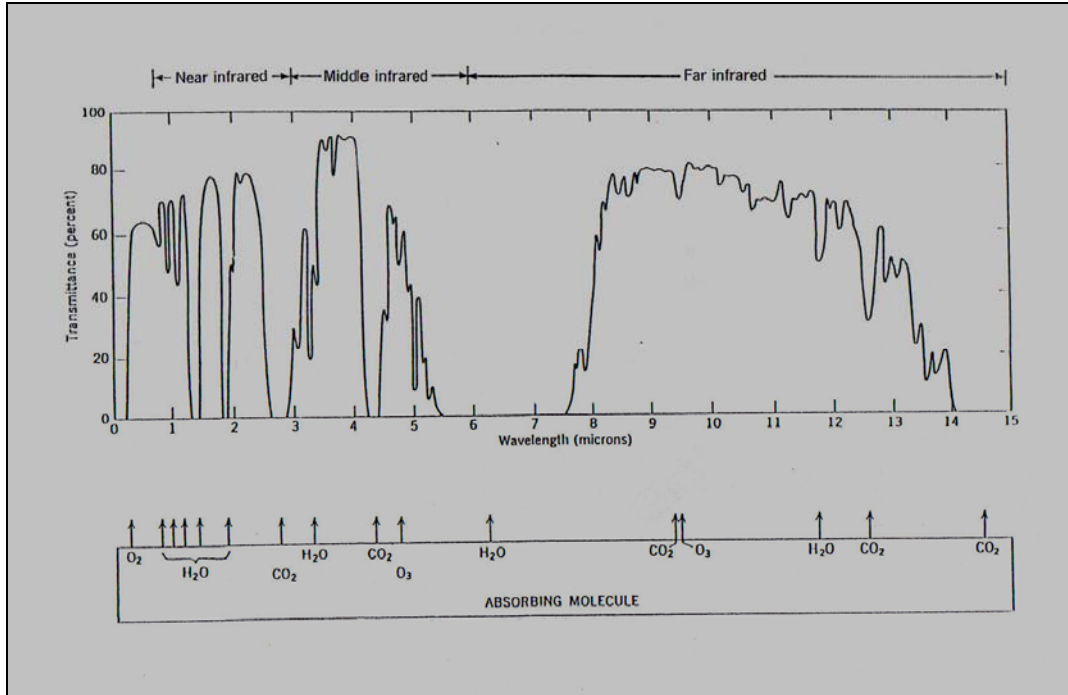


Figure 1. Transmittance of air and absorbing molecules by wavelength (From Ref. [1]).

Typically, detection within the spectrum of  $0.2 \mu\text{m}$  to  $1000 \mu\text{m}$  is considered optical detection [3]. Sensors within this optical region are limited to two main classes: photodetectors and thermal detectors. The time response for thermal detection is much slower because the absorbed radiation must cause a change in detector element temperature; as opposed to the generation of an electron-hole pair in photon detection [3]. The spectral response is also typically much broader for thermal detection. As a result, thermal detectors are primarily used in the Terahertz ( $10^{12}$  Hertz) region or where cooling requirements are not practical. Since these criteria do not apply for our particular application, a photon detection method is preferable for our design purposes.

Photodetectors can be broken down into three main categories: photovoltaic detectors, photoconductors, and photoemissive detectors [3]. These detectors consist of semiconductor devices or materials that incur parameter changes as a result of direct interaction with photons of light. This interaction within the atomic lattice of the material

creates changes in the resistance, inductance, voltage, or current within the device which can be detected by external circuitry. In the case of photovoltaic detectors, or photodiodes, changes in voltage or current result from optical radiation incident upon a semiconductor diode p-n junction. Photoconductors exhibit changes in resistance and conductance when optical radiation is applied. Photoemissive detectors use external photoelectric emission to detect light by emitting free electrons to a charged anode via an applied electric field [3]. Since quantum well photodetectors have characteristics most closely related to photoconductors, specifically extrinsic photoconductors, it may be beneficial to examine its properties more closely.

Photoconductors are comprised of a semiconductor material with ohmic contacts at opposite ends. Semiconductors have unique optical properties in which a photon ( $E=h\nu$ ) is absorbed within the atomic lattice of the material, exciting an electron in either a direct or indirect transition from the valance band to the conduction band, creating an electron-hole pair. In the example in Figure 2,  $E_g$  is the energy required to transition between valance and conduction bands, or bandgap energy, of the material. It is the charge carriers created by these electron-hole pairs that change the electrical properties of the material. In the case of photoconductors, these charge carriers are produced either intrinsically through band-to-band transitions, or extrinsically across forbidden gap energy states using doping atoms (Figure 3). Extrinsic photoconductors have only one type of charge carrier depending on doping type, and they must be cooled to liquid helium temperatures to prevent the ionization of carriers [8]. Once the device is illuminated by optical radiation, these charge carriers can be detected in the form of photocurrent using an external bias.

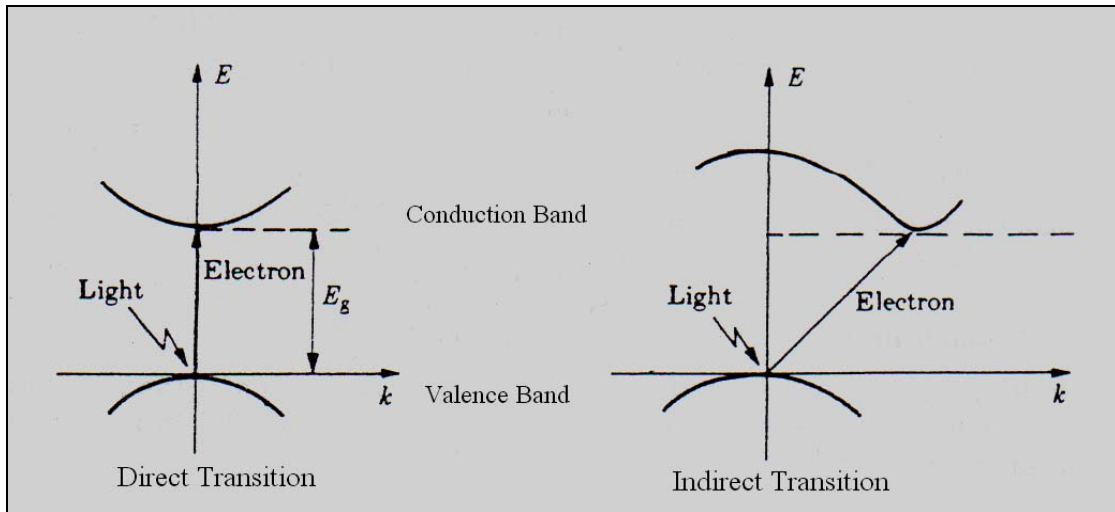


Figure 2. Creation of electron-hole pair by (a) direct and (b) indirect transition as a result of photon absorption (After Ref. [8]).

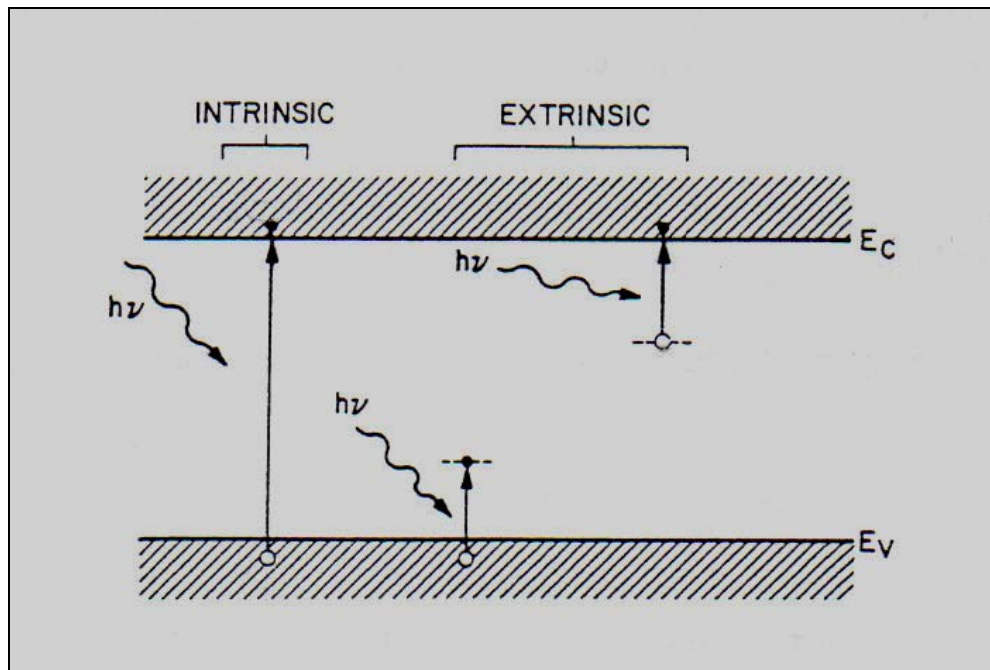


Figure 3. Intrinsic and extrinsic transitions with respect to a vertical energy profile (From Ref. [8]).

## B. THE QUANTUM WELL

As an alternative to the use of extrinsic photoconductive detection, a quantum well infrared photodetector (QWIP) can be used to detect infrared radiation with bandgaps outside the realm of normal semiconductor materials. This process involves making modifications to typical semiconductor devices, known as bandgap engineering, to create a new semiconductor material [10]. This new technology has been made possible through advances in molecular-beam epitaxy (MBE) and metal-organic chemical-vapor deposition (MOCVD), in which new semiconductor materials are grown one atomic monolayer at a time to predetermined specifications [3]. By layering different types of semiconductor materials in specific intervals and thicknesses, a heterostructure of large bandgap semiconductors is formed with absorption occurring within the quantized states. In this case, the absorption of photons occurs within the conduction or valence bands (intersubband) rather than across the energy gap (interband) as in conventional photoconductors [8].

The bandgap energy associated with each type of semiconductor material is related to the wavelength in which it absorbs by

$$E(eV) = \frac{1.24}{\lambda(\mu m)} \quad (1.1)$$

where  $E$  is the energy in electron-volts and the wavelength is given in micrometers [8]. In this way, the type of photon energy absorbed by interband transition can be manipulated by changing the type of semiconductor used. For example, the quantum well layer of GaAs seen in Figure 4 has a bandgap energy of approximately 1.4 eV and is surrounded by a bulk material of  $\text{Al}_{0.3}\text{Ga}_{0.7}\text{As}$  with a bandgap energy of 2.4 eV [8]. Absorption only occurs if the photon energy meets or exceeds the bandgap energy, so the quantum well effectively decreases the amount of photon energy required for absorption in the GaAs region compared to that of the bulk AlGaAs material. Due to the difference in the bandgaps of the two materials, the potential energy profiles of the conduction and valence bands will not be continuous. The potential well formed effectively traps the electron

within the barrier walls. The energy gap for the quantum well is related to the well thickness and approximately given by [11]

$$E_{QW} = E_g + \frac{\hbar^2 \pi^2}{2 m_r^* L^2} \quad (1.2)$$

where  $\hbar$  is Plank's constant,  $E_g$  is the bandgap energy of the well, and  $m_r^*$  is the reduced mass of the electron-hole pair. Therefore, the effective bandgap of the quantum well can be altered by controlling the thickness of the quantum well layer.

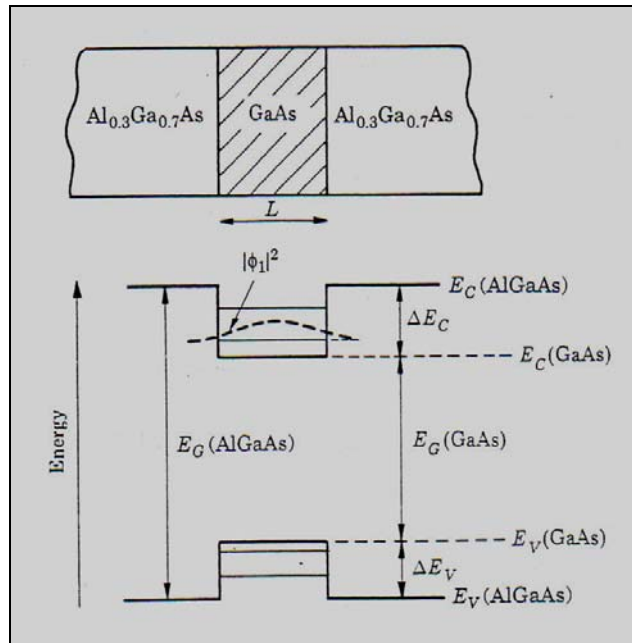


Figure 4. Example of quantized energy levels in a GaAs/AlGaAs quantum well (From Ref. [8]).

In intersubband transitions, electrons or holes are excited between quantized energy states located within the conduction or valance band, respectively. The heterojunction of the two different types of semiconductor materials create the potential well seen in Figure 5. When these potential barriers are sufficiently close together, as to approach the de Broglie wavelength of the electron, the number of available energy states is reduced and only discrete energy levels are present [3]. The state of the bound electron

can be approximately determined by the infinite square well approximation of the Schrödinger Wave equation

$$-\frac{\hbar^2}{2m_e} \frac{\partial^2}{\partial z^2} \psi_n = E_n \psi_n \quad (1.3)$$

where the wavefunctions and energy levels are given by

$$\psi_n(z) = \sqrt{\frac{2}{L}} \sin\left(\frac{\pi n z}{L}\right) \quad (1.4)$$

and

$$E_n = \left( \frac{\hbar^2 \pi^2}{2m_e L^2} \right) n^2 \quad (1.5).$$

In these equations,  $L$  is the width of the quantum well and  $n$  is the integer associated with each energy level [12]. In order for this approximation to be valid, the barrier width and height must be sufficiently large so that the electrons are tightly confined within the well. For finite quantum wells, the energy levels given in these equations will be slightly large so adjustments will need to be made using the finite well solutions.

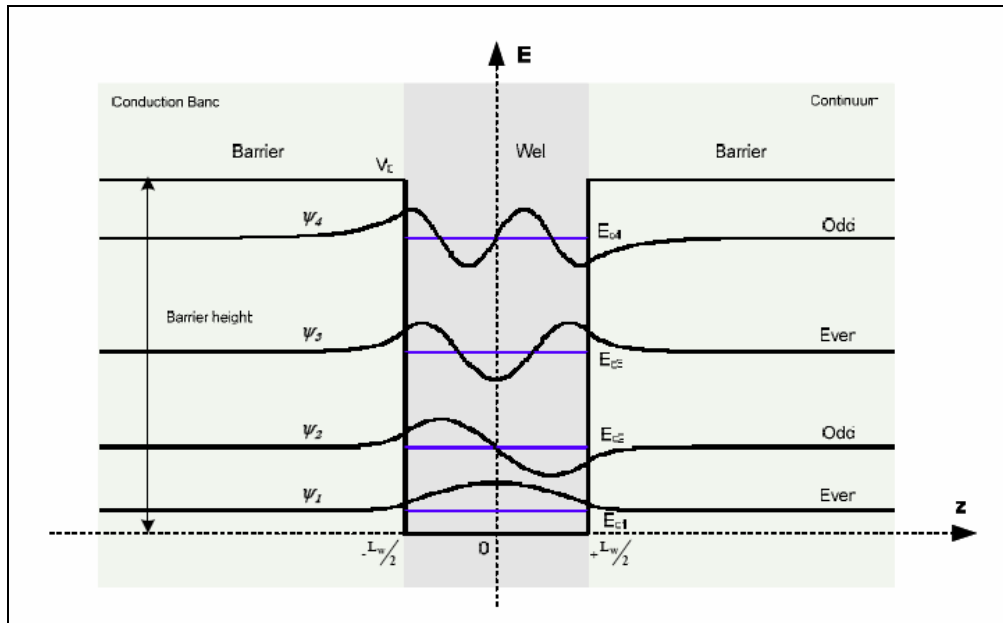


Figure 5. Discrete energy levels in a symmetric quantum well (From Ref. [1]).



For symmetric quantum wells, the strength of infrared absorption is given by the transition matrix element  $\langle \Psi_f | V_p | \Psi_i \rangle$ , where  $\Psi_i$  and  $\Psi_f$  are the initial and final wavefunctions, respectively and  $V_p$  is the photon interaction potential [8]. Based on the wavefunctions shown in Figure 5, it can be seen that only transitions between different parity states are permitted within the well. This is due to the fact that  $V_p$  in the dipole approximation contains the special coordinate  $z$  [8]. Therefore, transitions between states of the same parity are prohibited. That is to say that an electron can excite to the second energy level but not the third, and so on.

For efficient collection of photoexcited electrons, it is desirable to set the second energy level at the top of the potential well. In this way, the electron is excited from a bound state to continuum states within the conduction band and can contribute to the overall photocurrent of the system. Doping is required for these types of transitions to compensate for the lack of carrier transitions from the densely populated valance band to the sparsely populated conduction band. Therefore, the amount of photocurrent generated is limited by the amount of doping used. The photon energy required to make this transition can be determined using the quantized energy levels, and is far less than interband energy requirements for bulk semiconductor materials. Unlike photodetectors using interband transition, quantum well detectors are sensitive to a relatively narrow-passband spectral response due to resonant nature of intersubband transition [8]. By precisely manufacturing these devices, a detector can be made for a range of wavelengths, subject to the barrier height which depends on the bandgaps of the host materials.

While symmetric wells are very useful and provide adequate absorption for most intersubband transition based infrared detectors, the prohibition of interband transitions between states with different quantum numbers can limit some applications. For example, it may be desirable to have transitions occur between the first valance energy state and the second conduction energy state. In order to achieve absorption for this type of transition, symmetry within the well must be broken [8]. For these types of transitions, asymmetric quantum wells can be used to get the desired absorption wavelength (Figure 6).

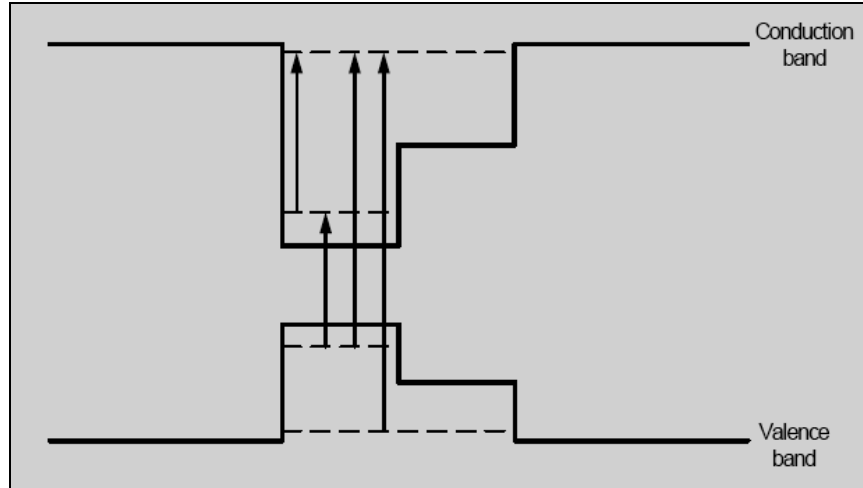


Figure 6. Example of an asymmetric well with allowable intersubband transitions  
(From Ref. [15]).

Multiple quantum well photodetectors consist of multiple layers of different semiconductor materials to increase quantum efficiency. The intersubband absorption occurs when polarization of the incident radiation has a component along the growth direction (Figure 7). Since the quantum well is grown vertically (z-direction), the polarization of light needs to have a component in the z-direction to satisfy the polarization selection rule [8].

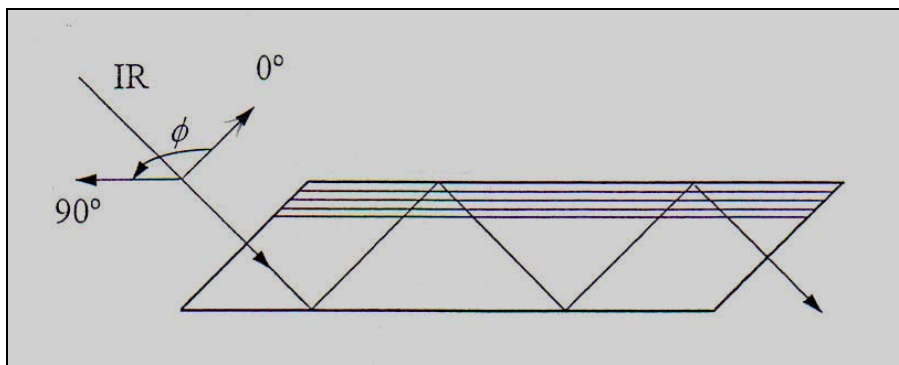


Figure 7. Incident angle of applied radiation for intersubband measurement as required by the polarization selection rule (From Ref. [8]).

The potential profile of the quantum well changes as a result of an external bias being applied to collect photoexcited electrons (Figure 8). In this case, the external bias creates a linearly sloping potential profile. This affects the overall operation of the device because thermally excited carriers can tunnel through the thinner top portions of the well where the barrier is not as thick.

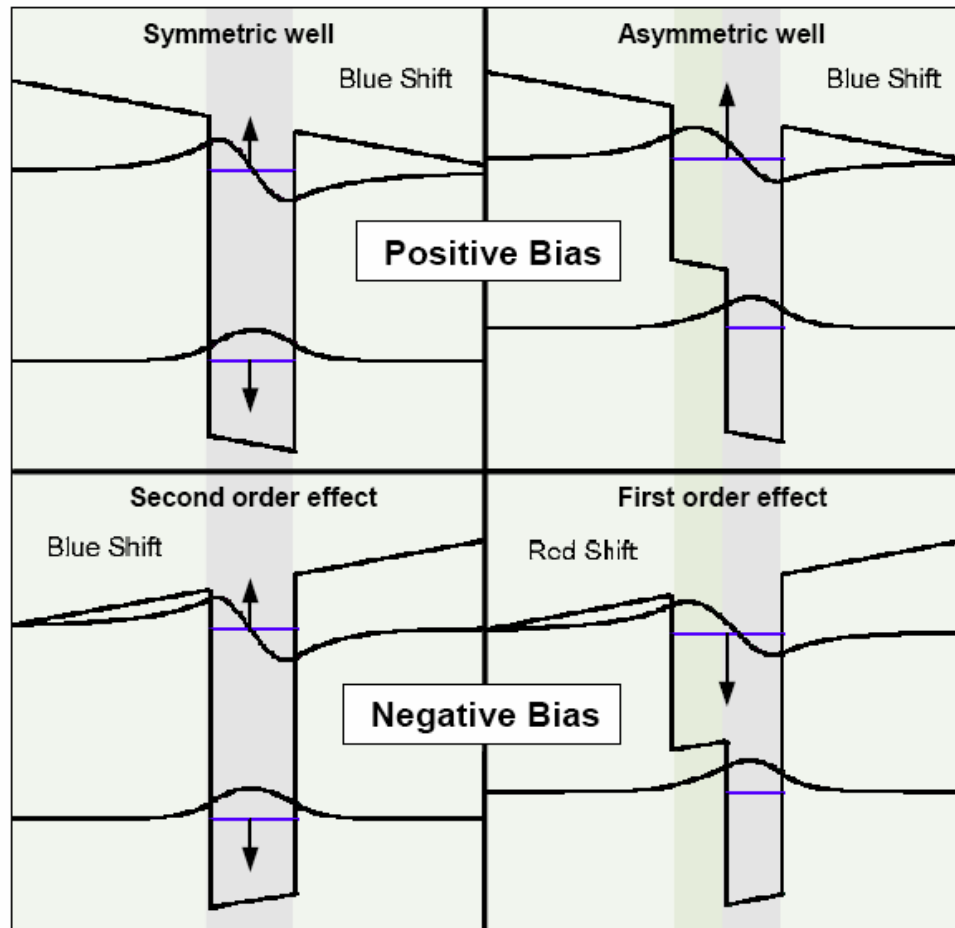


Figure 8. Effects of positive and negative biasing on symmetric and asymmetric wells  
(From Ref. [1]).

### C. MULTICOLOR INFRARED PHOTODETECTOR

Now that we have briefly discussed how quantum well infrared detectors work, I would like to introduce the multicolor infrared photodetector described in the first paragraph of this introduction. As stated earlier, this particular device was designed and sent for fabrication by Fabio Durante P. Alves as part of his Master's thesis.

The three-color QWIP described here is composed of three stacks of multi-layered InGaAs/GaAs/AlGaAs quantum wells grown vertically using the molecular-beam epitaxy process described earlier. Each stack, seen in Figure 9, consists of 20 different quantum well layers. The stacks are grown in the NIR, MWIR, and LWIR sequence from bottom to top in order to prevent undesirable absorption from occurring while infrared radiation is transitioning to each respective stack. Therefore, the larger bandgap materials are placed below the smaller bandgap materials. Contact layers are heavily doped (about  $2 \times 10^{18} \text{ cm}^{-3}$ ) and used to ensure contact uniformity in long pixels. Metal layers are used for wire bonding for the application of an external bias to each stack individually (Figure 10). As described earlier, a 45 degree angle is polished into the edge of the substrate to satisfy the polarization selection rule since no grating is applied in this device.

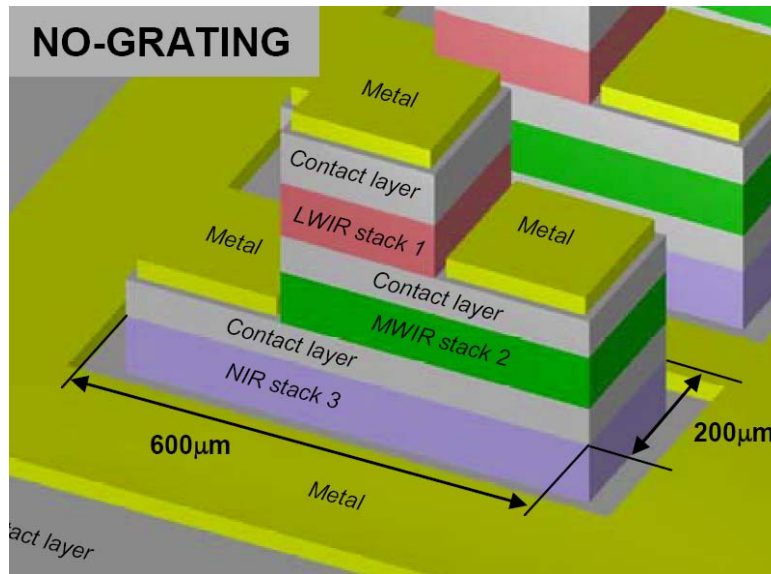


Figure 9. Physical structure of the multicolor detection device (From Ref. [1]).

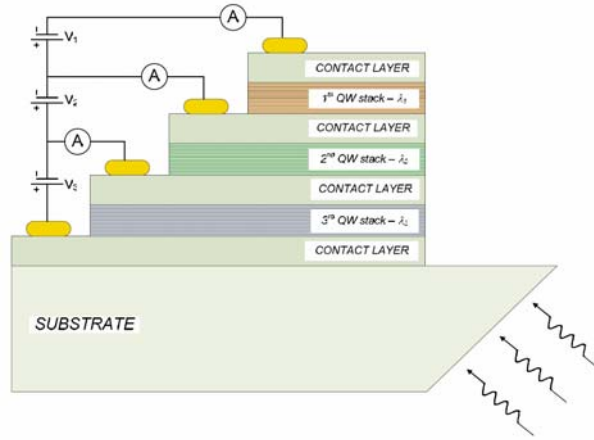


Figure 10. Structural diagram of device with angled incident radiation and external contacts applied (From Ref. [1]).

The potential profile for this particular detector is seen in Figure 11. The intersubband transitions between symmetric and asymmetric wells are used for LWIR and MWIR detection respectively, while the NIR detection is accomplished using interband transitions in an asymmetric well. A description of the composition of each layer shown, including doping concentrations, can be found in Table 1.

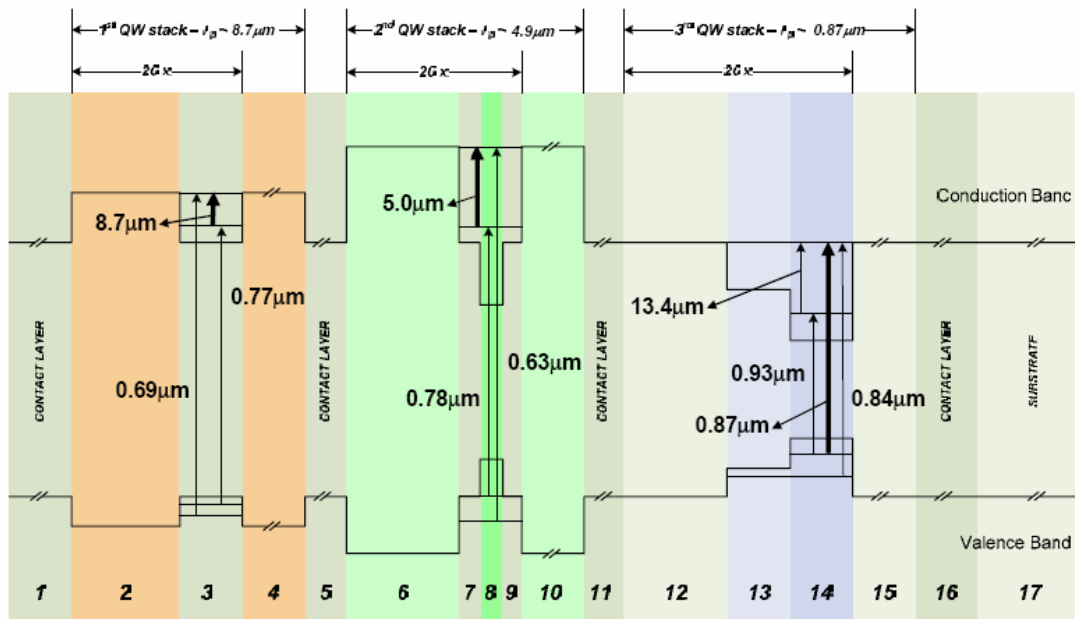


Figure 11. Potential profile for all three quantum well stacks (From Ref. [1]).

Table 1. Description of QWIP composition by layer (From Ref. [1]).

PROFILE		THICKNESS Å	DOPANT	CONC. ±10% cm <sup>-3</sup>
1	n-GaAs	7,000	Si	2x10 <sup>18</sup>
2	i-Al <sub>0.26</sub> Ga <sub>0.74</sub> As	300	None	-----
3	n-GaAs	52	Si	0.5x10 <sup>18</sup>
4	i-Al <sub>0.26</sub> Ga <sub>0.74</sub> As	300	None	-----
5	n-GaAs	5,000	Si	2x10 <sup>18</sup>
6	i-Al <sub>0.40</sub> Ga <sub>0.60</sub> As	300	None	-----
7	n-GaAs	13	Si	2x10 <sup>18</sup>
8	n-In <sub>0.15</sub> Ga <sub>0.85</sub> As	14	Si	2x10 <sup>18</sup>
9	n-GaAs	13	Si	2x10 <sup>18</sup>
10	i-Al <sub>0.40</sub> Ga <sub>0.60</sub> As	300	None	-----
11	n-GaAs	5,000	Si	2x10 <sup>18</sup>
12	i-GaAs	300	None	-----
13	i-In <sub>0.10</sub> Ga <sub>0.90</sub> As	43	None	-----
14	i-In <sub>0.25</sub> Ga <sub>0.75</sub> As	40	None	-----
15	i-GaAs	300	None	-----
16	n-GaAs	7,000	Si	2x10 <sup>18</sup>
17	S.I. GaAs Substrate	-----	-----	-----

The bottom stack is 200  $\mu\text{m}$  by 600  $\mu\text{m}$  in size and is designed to absorb NIR radiation at about 0.87  $\mu\text{m}$ . The transition between the first valance energy state and the second conduction band energy state is the major contributor for photocurrent, due to the calculated position of the second state. Since this is an interband transition, no doping was used in the quantum well. The concentration of indium is limited within the well layer due to growth restrictions and lattice mismatch considerations [1].

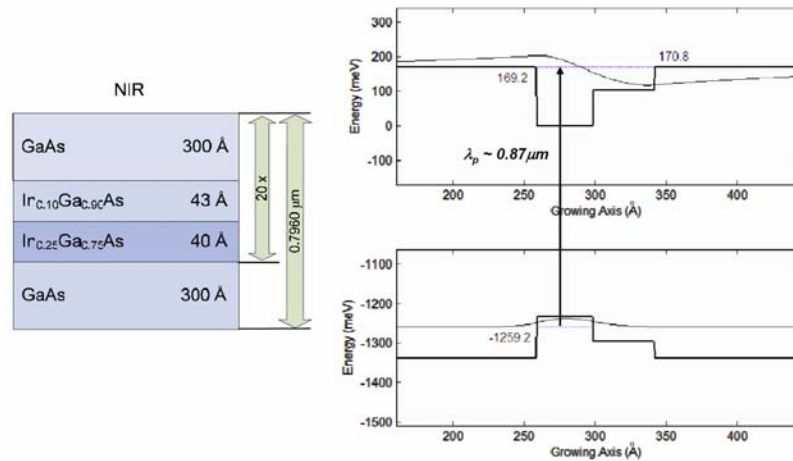


Figure 12. NIR detector potential profile and layer description (From Ref. [1]).

The second stack is 200  $\mu\text{m}$  by 400  $\mu\text{m}$  in size and is designed to detect MWIR radiation at around 4.9  $\mu\text{m}$ . In this case, the major transition component comes from an intersubband transition within an essentially symmetric well. The asymmetric aspect of this well is due to the placement of two layers of GaAs on either side of the  $\text{In}_{0.25}\text{Ga}_{0.75}\text{As}$  to accommodate the lattice mismatch [1].

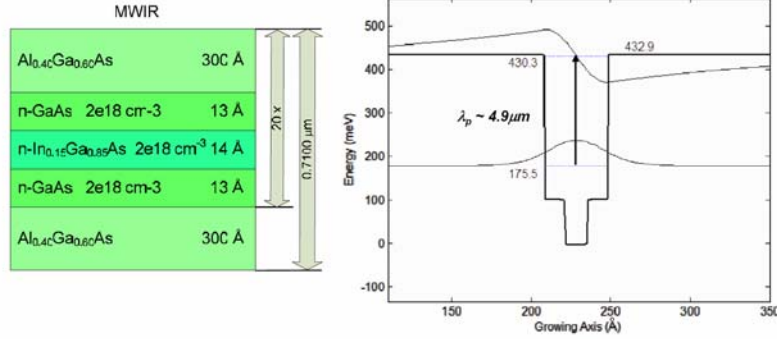


Figure 13. MWIR detector potential profile and layer description (From Ref. [1]).

The top stack is 200  $\mu\text{m}$  by 200  $\mu\text{m}$  in size and is designed to detect LWIR radiation at about 8.7  $\mu\text{m}$ . For this symmetric well intersubband transition, doping concentrations were reduced to minimize the potential for unwanted low energy thermionic emissions [1].

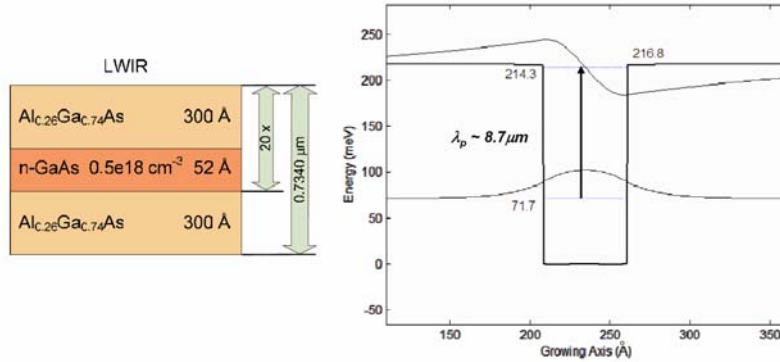


Figure 14. LWIR detector potential profile and layer description (From Ref. [1]).

A plot of energy bandgaps vs. lattice constants is shown in Figure 15. As we have already discussed, the matching of lattice constants between layers can be an important part of the overall structure design. The types of materials used ultimately determine the amount of strain internal to the crystalline structure, the number of layers permissible, and the growth techniques used.

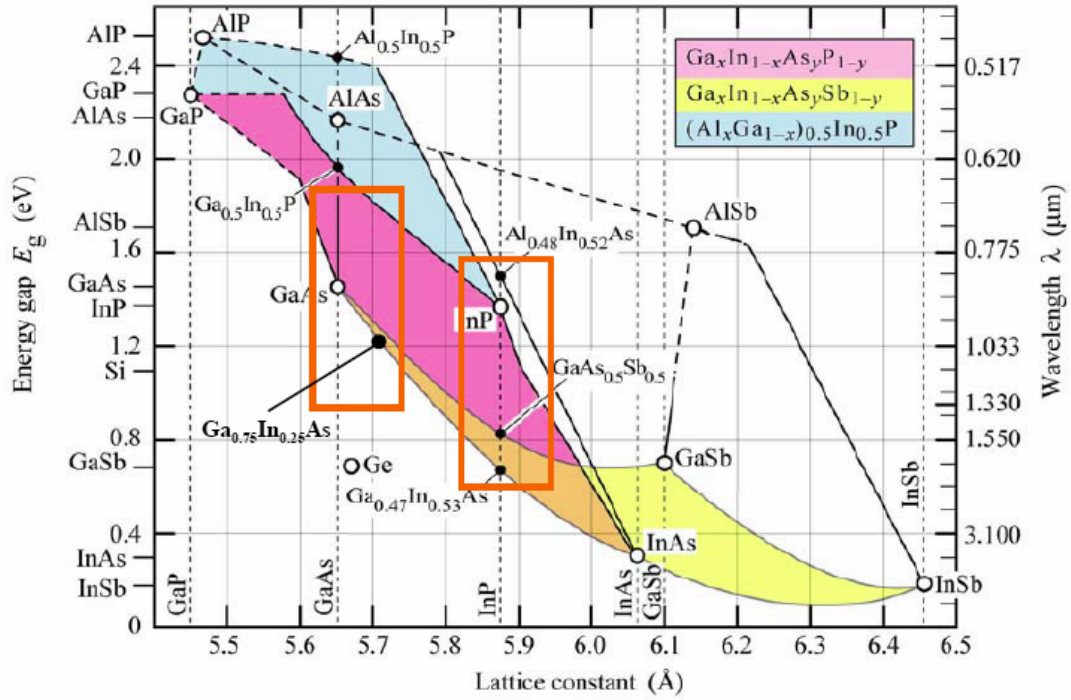


Figure 15. Plot of energy bandgap vs. lattice constants for major III-V compounds  
(After Ref. [14]).



THIS PAGE INTENTIONALLY LEFT BLANK

## **II. I-V CHARACTERISTICS**

### **A. I-V MEASUREMENT**

Current-voltage (I-V) measurements were taken for a wide range of temperatures with no incident radiation applied in order to determine the dark current associated with each device. For this measurement, the detectors were mounted on a closed-cycle refrigeration unit capable of controlling the temperature in the 10-350 K range. Using this I-V data, the optimum operational range and limitations of each detector can be determined. This data can then be used to calculate the effective barrier heights within each well type, the background limited infrared performance (BLIP), and temperature dependence on leakage current [6].

There are several sources of dark current that are to be expected in a quantum well detector. At low temperature, the dominant source of dark current is caused by sequential resonant tunneling [13]. This effect is random and independent of temperature, and it is the source of many of the fluctuations seen at low dark current levels. As temperature increases, thermal excitations assist in the tunneling process by exciting the electrons closer to the tip of the sloping barrier wall. At high temperatures, classic thermionic emission is the dominant source of dark current and increases exponentially with temperature. In order to minimize these unwanted sources of dark current, thicker barrier layers, larger energy transitions between first and second energy state, and reduction in doping concentrations must be considered in the design of the device. As with every working device, compromises between sensitivity and output signal power need to be made.

## **B. EXPERIMENTAL RESULTS**

For this experiment, an external bias was applied to each of the three stacks individually with no IR radiation applied. The first test was done with cold aluminum foil surrounding the device to shield the background infrared radiation. For the second, the aluminum cover was removed to determine the extent to which background levels affect performance. The I-V data was collected using an Agilent 4155B semiconductor parameter analyzer. The operational process of this analyzer can be found in Appendix A.

### **1. Near Infrared Detector**

Figure 16 shows the measured I-V characteristics for the near infrared detector as a function of temperature with the cold aluminum shield in place. The clutter seen at low bias is most likely due to limitations on analyzer sensitivity levels. At high bias ( $\pm 4.5\text{V}$ ), the background current rises drastically due to field assisted tunneling of electrons through the barrier formed between the doped contacts and the undoped multiple quantum well structure. There is no real temperature dependence on the background current, which is expected because no doping is used for this interband transition. However, we do see a slight dip in current for temperatures below 50K at high bias, and further studies are needed to understand its origin.

The I-V curve at 10K without the aluminum foil can be seen in Figure 16 as a dashed red line, with temperature dependence shown in Figure 17. For NIR detection, the photogenerated current due to background light (or BLIP) is the dominant source of dark current at any temperature within the bias voltage ranges applied. As expected, temperature dependence and thermionic emissions are not a major factor in the open detector experiments as well.

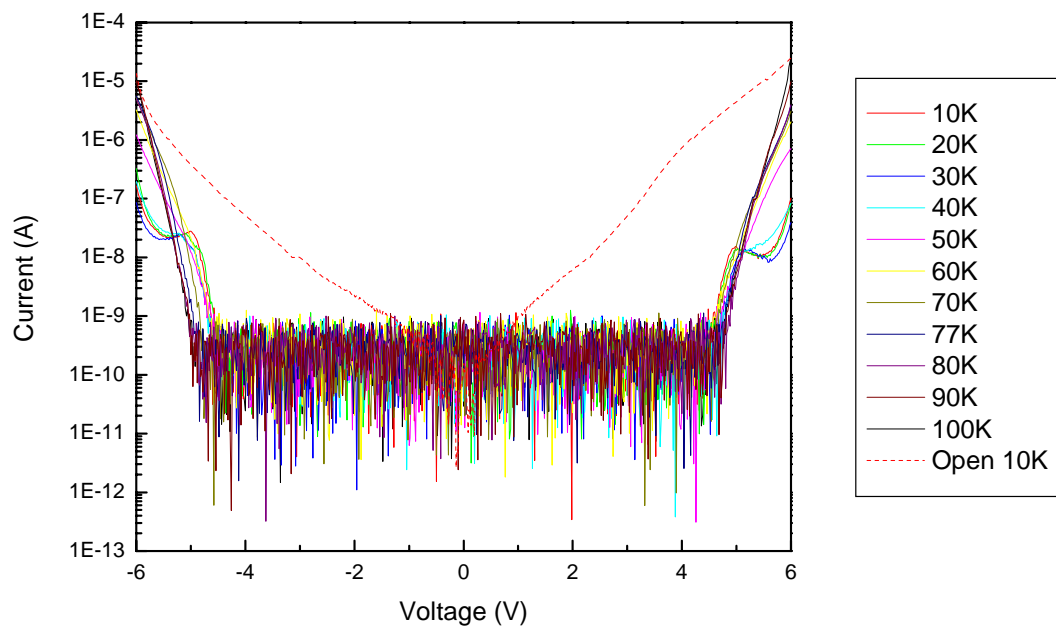


Figure 16. NIR detector I-V curves with cold aluminum shield. The dashed red curve corresponds to I-V without the shield at 10 K.

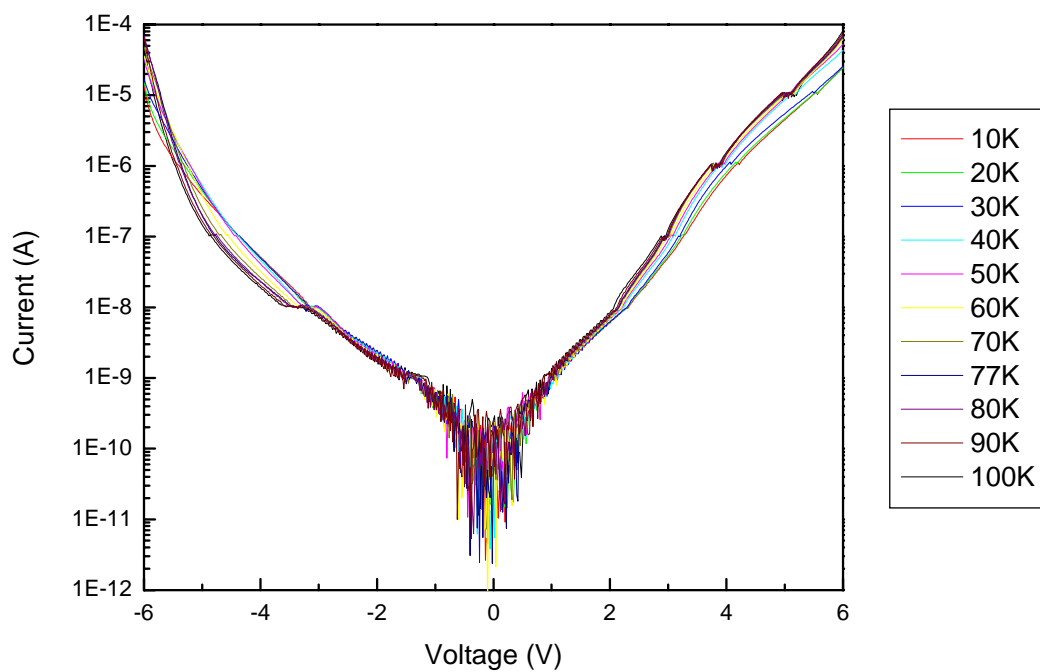


Figure 17. NIR detector I-V curves without the aluminum shield.

## **2. Mid-Wavelength Infrared Detector**

The MWIR detector has heavily doped quantum wells, and strong temperature effects are expected in the I-V characteristics. However, the thermal energy required to excite an electron out of the well is much greater than that of the LWIR detector so the differences in dark current vs. temperature should not be as drastic. As seen in Figure 18, dark current within the cold shield begins to increase almost immediately at high temperatures ( $> 80$  K) due to the thermionic emission. At low temperatures ( $< 80$  K) dark current is primarily due to thermal assisted tunneling and sequential tunneling [11]. Each curve shows an exponential increase in dark current with bias once an initial threshold is overcome. Once again, the 10 K data without the shield has been plotted in Figure 18 in order to determine the BLIP of the detector. In this case, cooling below 80K is unnecessary unless the device is operating at a very large external bias voltage. However, this device is operating in conjunction with the other two detectors, and the ultimate operating temperature will be determined by the BLIP of the LWIR detector since it has the lowest barrier for thermionic emission.

The I-V curves without the cold shield, shown in Figure 19, resemble those in Figure 18 with the exception that dark current begins to increase immediately with applied bias for all temperatures. At low temperatures ( $< 50$  K), the current primarily comes from the photoexcited electrons generated by the background infrared radiation. At high temperatures ( $> 50$  K) thermionic emission and thermal assisted tunneling also contribute to the current generated by the background.

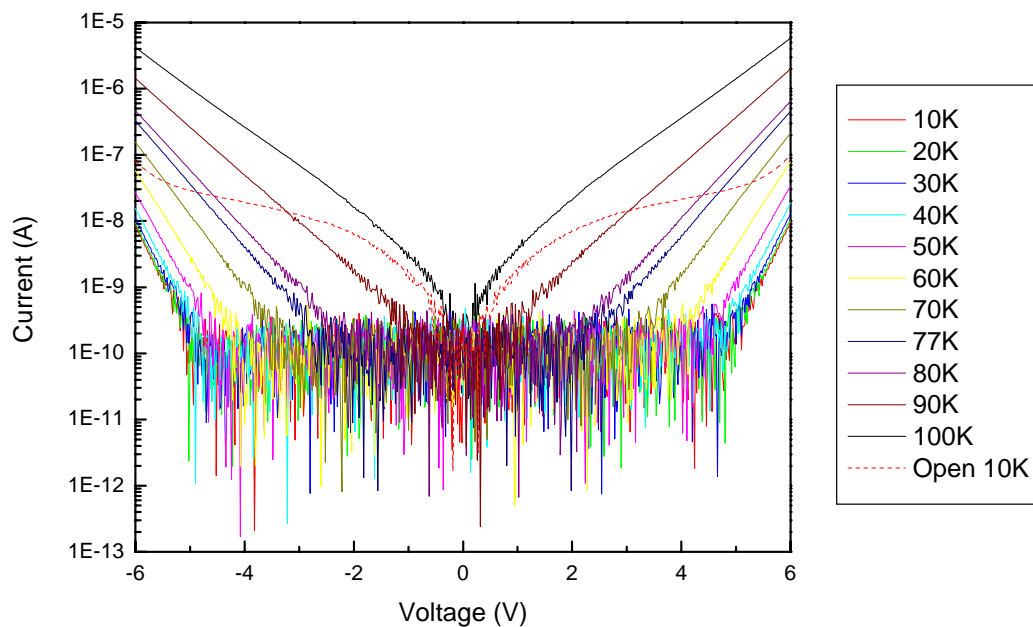


Figure 18. MWIR detector I-V curves with cold aluminum shield. The dashed red curve corresponds to I-V without the shield at 10 K.

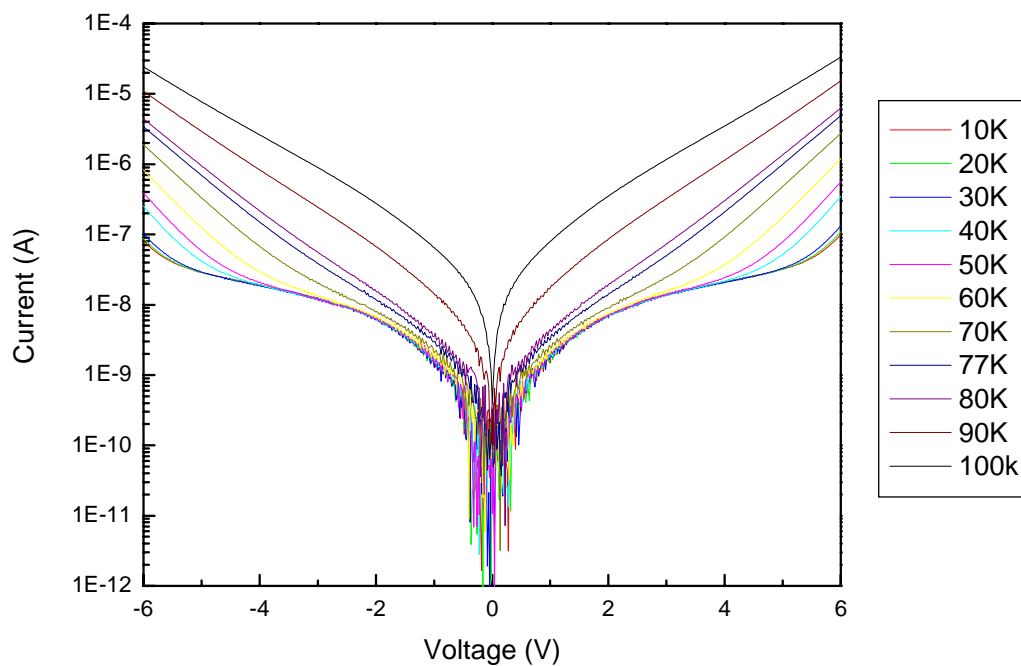


Figure 19. MWIR detector I-V curves without the aluminum shield in place.

### 3. Long-Wavelength Infrared Detector

The LWIR detector I-V curves shown in Figure 20 show a dramatic, and almost immediate, increase in dark current with temperature. This is expected and largely due to smaller barrier heights associated with the LWIR detector. The dark current can be reduced by lowering the doping density in the quantum wells, which reduces the quantum efficiency. A compromise had to be made between large leakage current (high doping concentration) and smaller detector signal.

The BLIP for this device shows an operating temperature of about 70 K. This will not allow the use of liquid nitrogen (77 K) for cooling as commonly used in conventional infrared detectors. The other limitation on this detector will be the levels of external bias voltage applied. The bias should be kept to a minimum without significant loss of detector signal. The details of bias dependence on detector operation will be discussed further in the next section.

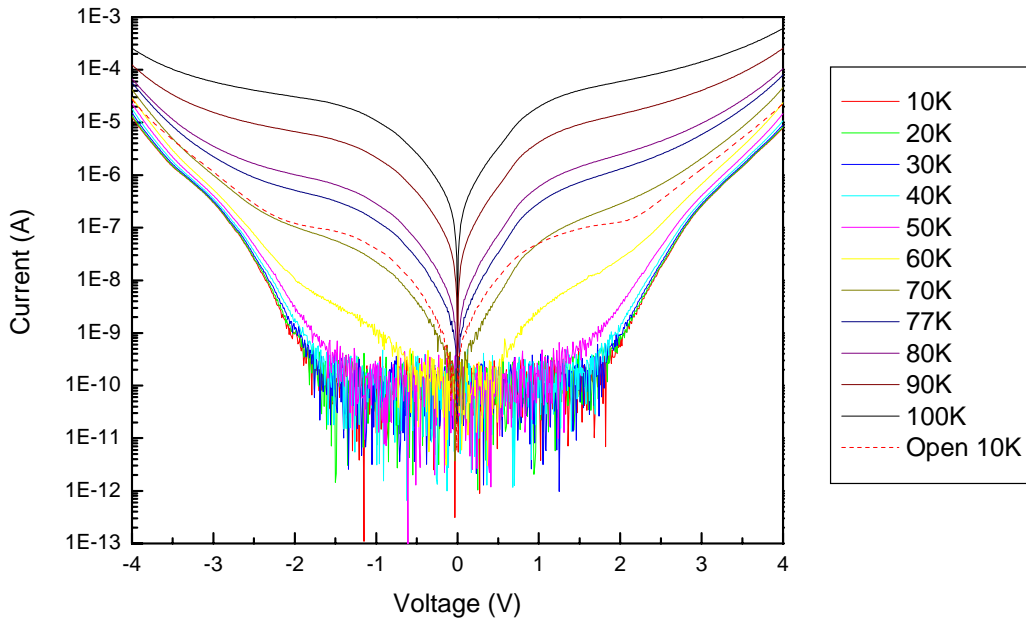


Figure 20. LWIR detector I-V curves with cold aluminum shield. The dashed red curve corresponds to I-V without the shield at 10 K.

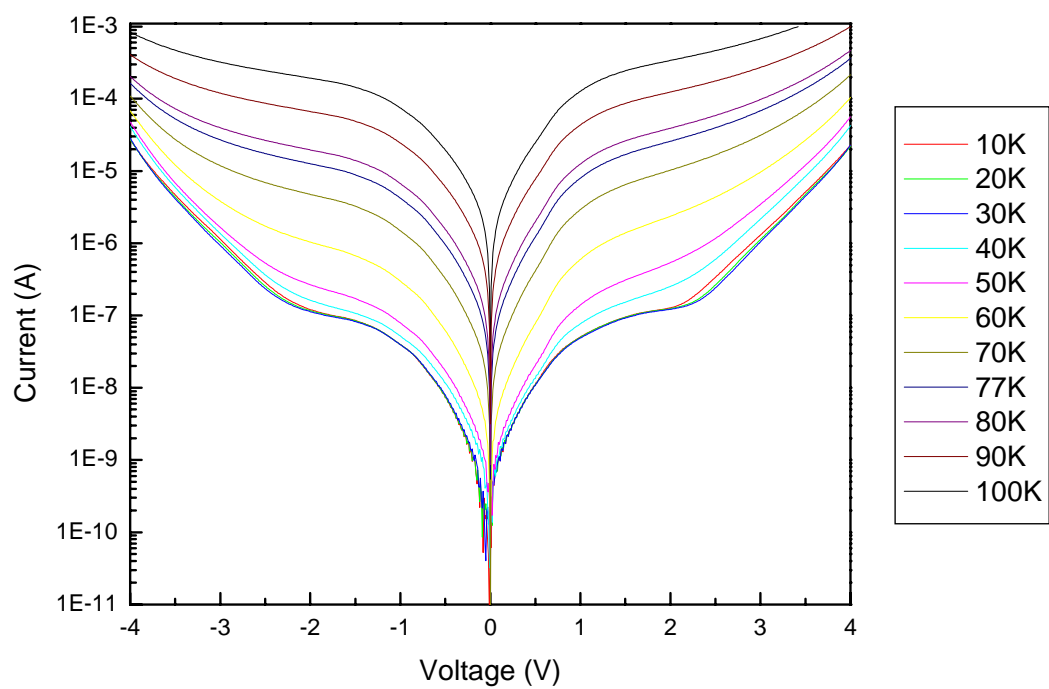


Figure 21. LWIR detector I-V curves without the aluminum shield.



THIS PAGE INTENTIONALLY LEFT BLANK

### **III. PHOTOCURRENT MEASUREMENT**

#### **A. INTRODUCTION**

Photocurrent measurements allow us to analyze how the detector performs at various wavelengths under different operating parameters, such as bias and temperature. In addition, these measurements allow the determination of key figures-of-merit including detection wavelength band and responsivity. The data provides information for determining optimized temperature and bias operating values.

##### **1. Experimental Setup**

The experimental setup used for photocurrent measurement is depicted in Figure 22. An Oriel 6363 resistive heating element was used as a long wavelength infrared radiation source, and an Oriel 6333 Quartz-Tungsten-Halogen (QTH) lamp was used for NIR. The incident light was sent through a computer actuated filter-wheel assembly to remove second order diffraction effects. The IR beam was then sent to a monochromator, which specifies the wavelength of radiation to be sent to the device using a series of gratings and mirrors. This narrow range of wavelengths was sent through an optical chopper, which modulates the signal and allows the lock-in amplifiers to filter out ambient noise. Two slits, located at the input and output of the monochromator, were used to adjust the beam size for optimizing signal and wavelength resolution. The slit widths used in this experiment were 2 mm unless otherwise stated.

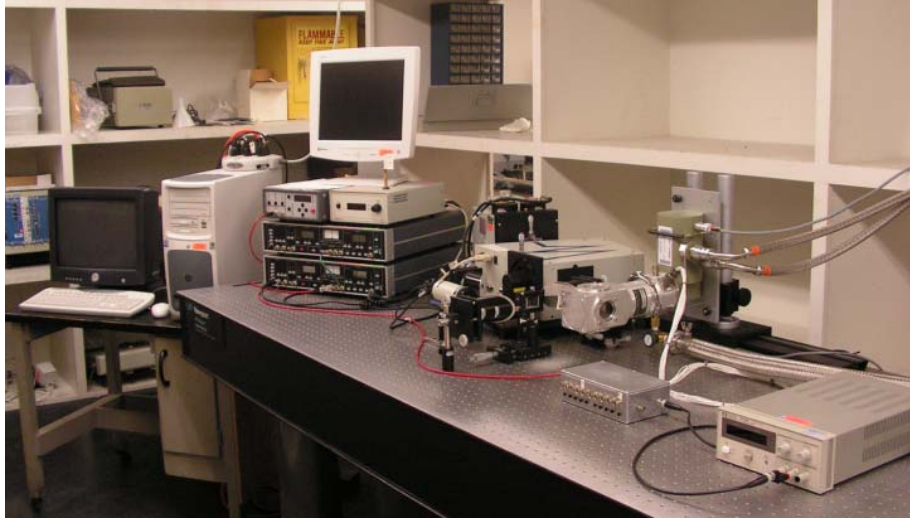


Figure 22. Photograph of photodetector characterization system setup.

Once a narrow band IR beam has been established, it is sent via mirrors to a gold plated beam splitter (Figure 23). Half of the incident radiation is sent to a reference detector to calculate flux power. Simultaneously, the other half is sent to the cooled detector. The reference detector is used to minimize errors arising from temporal variations in incident light intensity due to atmospheric absorption and blackbody tendencies with the IR source. Both inputs are used to calculate the responsivity of the device.

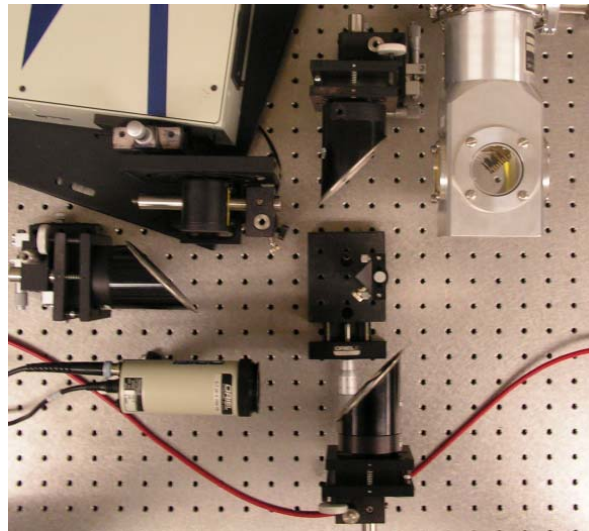


Figure 23. Mirror and beam splitter assembly with reference (bottom left) and cooled (top right) detectors shown.

## 2. Converting Photocurrent to an Electrical Signal

Using an external power supply via the junction box seen in Figure 24, a bias is applied across each quantum well stack individually. The electric field generated due to the applied bias supplies photoexcited electrons with the drift velocity needed for a photocurrent to become established. As the narrow band, modulated IR beam illuminates the device, electrons are excited out of there individual wells and contribute to the photocurrent in the system. This current is detected using a lock-in amplifier (Figure 25) which amplifies the signal a million times and displays it on the digital readout.

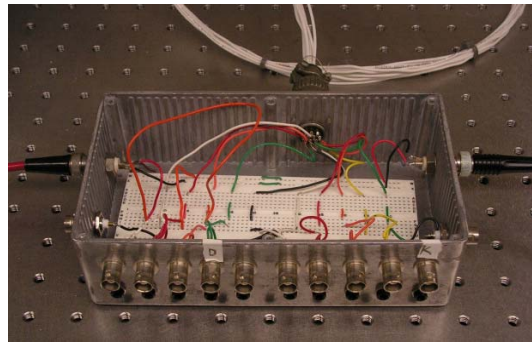


Figure 24. External bias junction box.

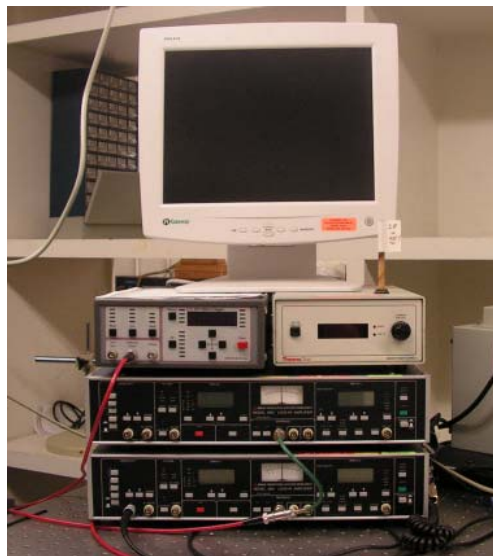


Figure 25. Lock-in amplifiers for photocurrent and reference voltage measurement.

A majority of this photodetector characterization system was constructed by Bryan Herdlick as part of his Master's research project [5]. A LabView program was used to automate the filter/grating selection and monochromator operation processes. This program allows us to run “scans” at specified wavelength intervals without any manual manipulation to the system. The software is also linked to the lock-in amplifiers to extract signals from the sample and reference detectors (For more information on LabView or equipment specifications, see Ref. [5]). For each scan, a time delay of five seconds was implemented between each data point to ensure steady-state values were recorded.

### 3. Calculating and Interpreting Responsivity

The responsivity for each detector is calculated using the reference and detector signals recorded over the course of each scan. The reference detector output voltages were used to determine the beam flux power incident on the test device at each wavelength interval. The infrared power incident on the reference detector,  $\Phi_R$ , and its output voltage,  $V_R$ , are related by [8]

$$\Phi_R = \frac{V_R}{R_R} \quad (3.1)$$

where  $R_R = 1000 \text{ V/W}$  is the responsivity of the reference detector. This responsivity value is nearly independent of wavelength in the 0.8 to 35  $\mu\text{m}$  range. Using (3.1), the beam intensity,  $I_R$ , can be found as

$$I_R = \frac{\Phi_R}{A_R} \quad (3.2)$$

where the area of the detector,  $A_R$ , is 10  $\text{mm}^2$  (dependent on the slit width of the monochromator). The responsivity of the test detector,  $R_{\text{Det}}$ , can then be calculated using area of the detector,  $A_{\text{Det}}$ , as follows:

$$\Phi_{\text{Det}} = I_R (A_{\text{Det}}) \quad (3.3)$$

and

$$R_{Det} = \frac{I_{Det}}{\Phi_{Det}} \quad (3.4)$$

where  $I_{Det}$  is the measured photocurrent from the test detector, which depends on the wavelength of incident infrared radiation. Note that the responsivity values must be adjusted for reflection losses at the ZnSe window of the cryostat and at the substrate of the detector, as well as the increase in path length in the quantum well structure due to the 45° incident angle of radiation described earlier. For the purpose of this experiment, this means dividing the detector responsivity by approximately 0.8. In addition, note that the detector area changes depending on the three wavelength ranges (dimensions can be seen in Figure 9). In order to take into account the temporal changes to the signals from background variations, a shutter was used before and after each scan to determine the average level of background signal. This average value, for both reference voltage and test detector current, was then subtracted from the overall signal to remove the background effects. In this way, the responsivity values given in the remainder of this section are an accurate reflection of actual detector performance.

## **B. BIAS DEPENDANCE OF RESPONSIVITY**

In this section, the external bias dependence of responsivity in each detector is analyzed. Forward and reverse bias dependence are both considered, and similarities and differences of each will be explained. Each scan was conducted at a temperature of 10 K. For all measurements taken, positive (forward) bias refers to the positive terminal being applied to the top of each mesa.

### **1. Near Infrared Detector**

The NIR photocurrent responsivity was measured using both IR and visible sources. However, measurements taken using the IR source were unreliable due to lock-in amplifier saturation conditions, so only measurements taken using the visible light source will be shown here. Each scan was conducted within a wavelength range of 0.75

$\mu\text{m}$  to  $1.05 \mu\text{m}$  at  $0.005 \mu\text{m}$  steps. The average reference detector background voltage in this region was slightly less than  $4 \text{ mV}$ , and the test detector leakage current was minimal due to the lack of doping in the quantum wells. Figure 26 shows the responsivity of the NIR detector at  $10 \text{ K}$  for a set of bias voltages. The slit width was reduced to  $0.5 \text{ mm}$  to limited incident power for avoiding the saturation of the lock-in amplifier. The short wavelength cutoff of the responsivity at around  $0.83 \mu\text{m}$  is due to absorption of incident light by the substrate. The responsivity peaks at about  $0.85 \mu\text{m}$  with a  $2.25 \text{ V}$  external bias applied, and then is drastically reduced. This reduction is most likely due to shifting from a nearly bound first excited electron state to the continuum, which can affect the strength of the transition. The initial increase of responsivity with bias is primarily due to increase of drift velocity of carriers with bias.

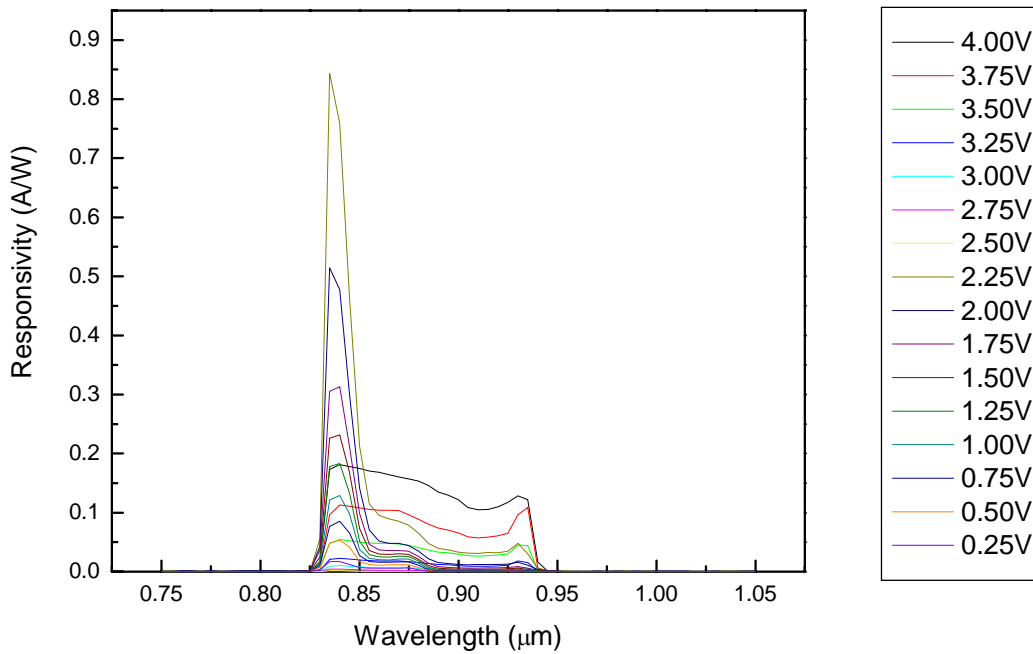


Figure 26. Responsivity as a function of wavelength of the NIR detector for a set of forward bias voltages using the visible light source.

In both the forward (Figure 26) and reverse (Figure 27) bias responsivity plots, interband transitions to multiple states can be seen with positions in agreement with the theoretical values given in Figure 11. It is interesting to note that this detector was

designed for a primary transition at 0.87  $\mu\text{m}$ . However, it appears that the 0.84  $\mu\text{m}$  transition between the second valance energy state and the second conduction band energy state is the preferred excitation mechanism due to the effective symmetry of the well.

The reverse bias responsivity is comparable to that of the forward bias, which creates an almost perfect mirror image. However, the peak responsivity value in the reverse bias measurement is about 33% greater and attributes the asymmetry of interface qualities during the MBE growth [11].

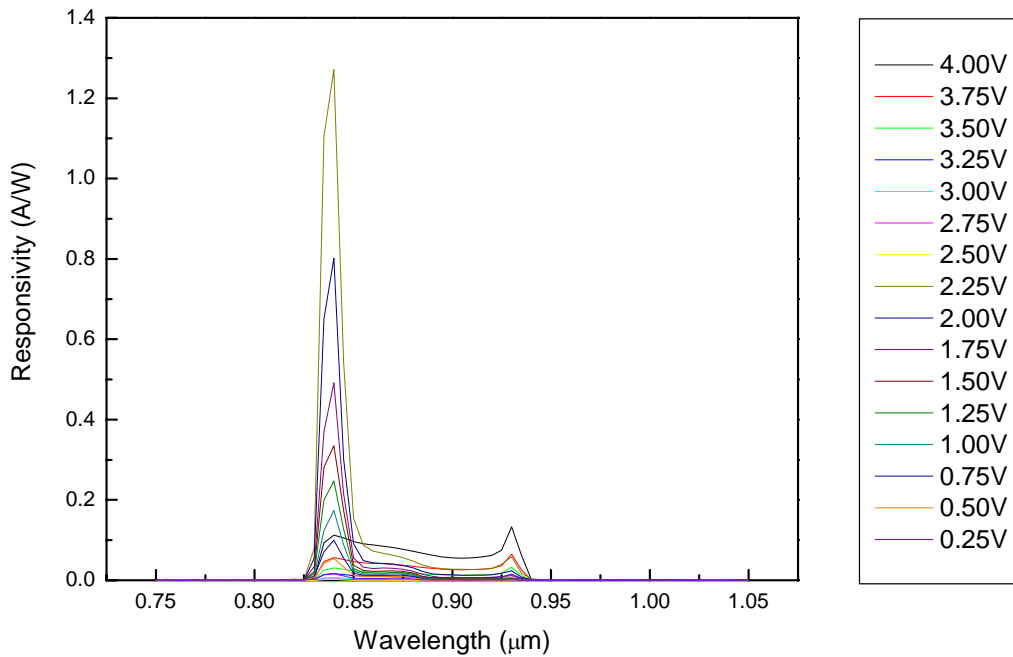


Figure 27. Responsivity as a function of wavelength of the NIR detector for a set of reverse bias voltages using the visible light source.

## 2. Mid-Wavelength Infrared Detector

The MWIR scan was conducted over a wavelength range of 4  $\mu\text{m}$  to 6  $\mu\text{m}$  at 0.025  $\mu\text{m}$  steps. The average background reference detector voltage was around 4 mV in this region, with an average background test detector current of approximately 0.01 nA.



The background current, in this case, was found to be bias dependent. The designed transition wavelength for this detector was about 4.9  $\mu\text{m}$ , but the forward (Figure 28) and reverse (Figure 29) measurements show a slightly longer value. This is probably due to approximations made in barrier height or slight fabrication uncertainties. The spikes in responsivity seen at around 5.4  $\mu\text{m}$  wavelength values in both measurements are due to a filter change at the same position.

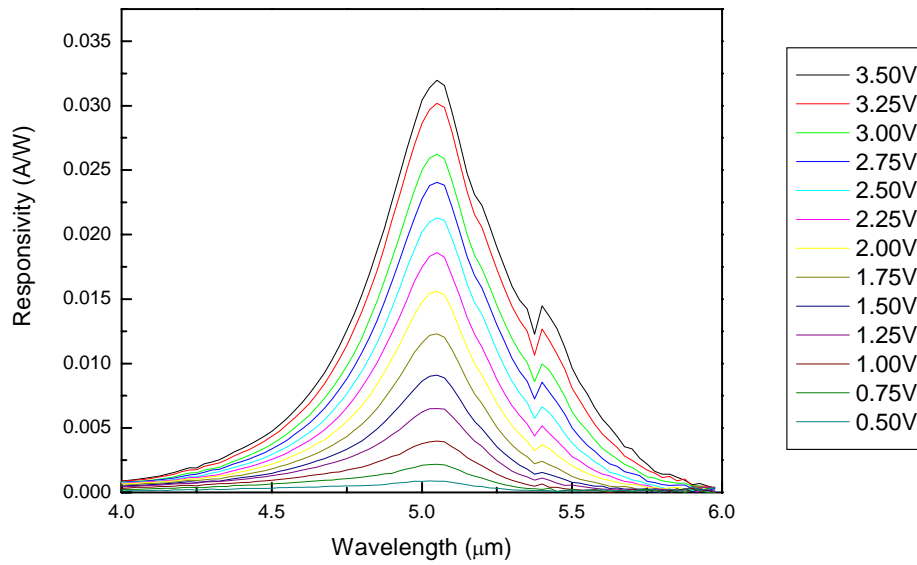


Figure 28. Responsivity as a function of wavelength for the MWIR detector for a set of forward bias voltages.

The MWIR forward bias measurement shows only a slight blue shift to the left, while the reverse bias leftward shift is more apparent. Such a shift is primarily due to the Stark effect in symmetric quantum wells observed previously by Harwit and Harris [4].

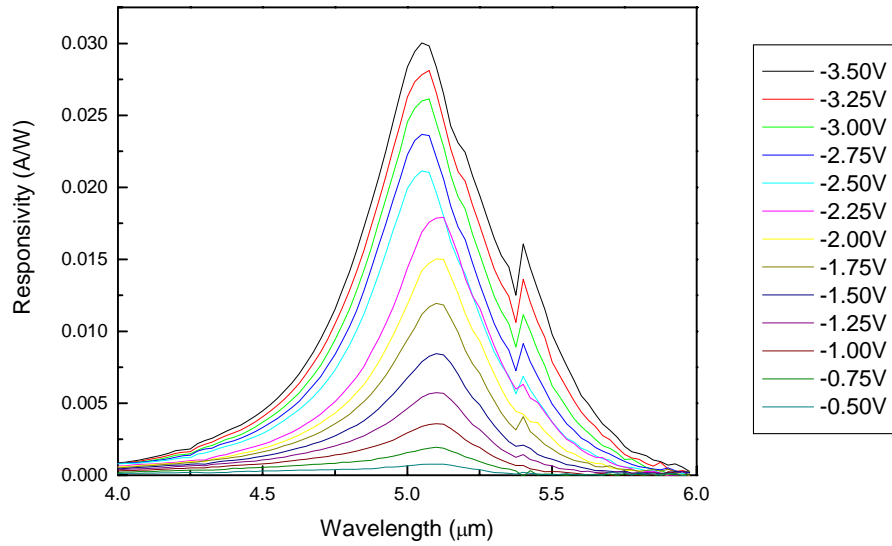


Figure 29. Responsivity as a function of wavelength for the MWIR detector for a set of reverse bias voltages.

### 3. Long-Wavelength Infrared Detector

For the LWIR detector measurements, a scan was conducted over a 6  $\mu\text{m}$  to 11  $\mu\text{m}$  range at 0.05  $\mu\text{m}$  intervals. The average reference detector background voltage was around 4 mV, with an average test detector background current of approximately 0.04 nA. The higher background current is due to peaking of 300 K blackbody radiation around 10  $\mu\text{m}$ , which provides more photons in the above range. As with the MWIR measurements, the test detector background current is bias sensitive. The responsivity curves for forward and reverse bias LWIR detection are shown in Figure 30 and Figure 31, respectively. Recall that for the LWIR detector, the doping concentrations in the GaAs well layer were reduced to minimize unwanted thermionic emissions. A compromise had to be made between large leakage current and poor photocurrent output. The effects of these compromises can be seen below.

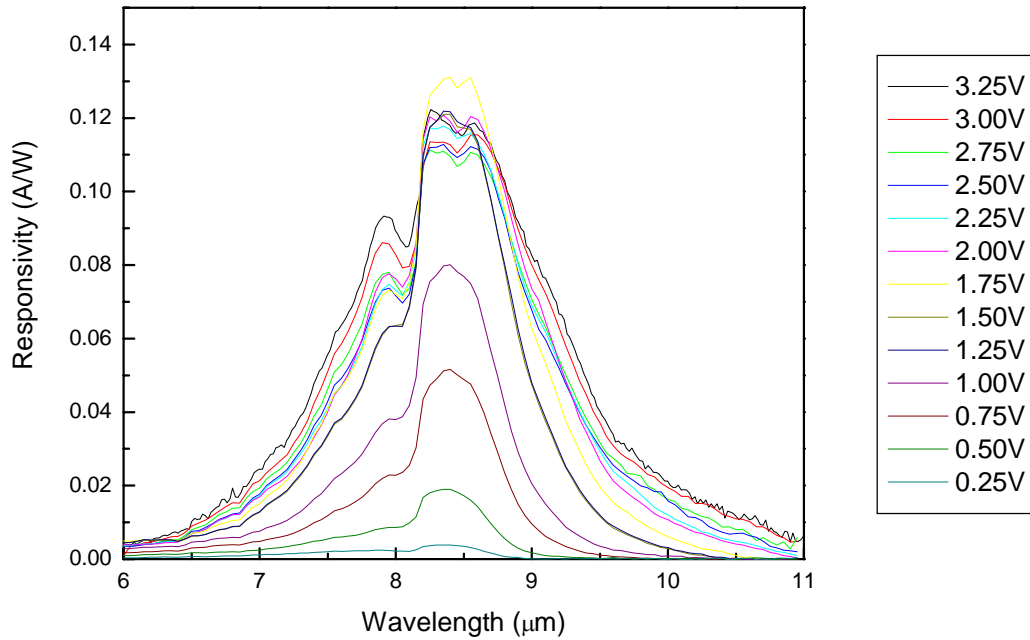


Figure 30. Responsivity as a function of wavelength for the LWIR detector for a set of forward bias voltages.

The peak responsivity values measured in LWIR detection were about 0.13 A/W and 0.16 A/W for forward and reverse bias respectively. A reduction in doping concentration limits the number of charge carriers present for photoexcitation. At high bias, saturation of responsivity is primarily due to the saturation of drift velocity of electrons [11].

Like the previous two detectors, there is a slight difference between expected wavelength absorption values and the values measured here. Specifically, this detector was designed to detect 8.7  $\mu\text{m}$  wavelength radiation, but the peak responsivity values show an absorption wavelength of about 8.4  $\mu\text{m}$ . This variation is most likely due to the asymmetric nature of the well or fabrication uncertainties, but further measurements are needed to determine its true origin.

Reverse bias responsivity is slightly higher than the responsivity found for forward bias as observed for the MWIR detector. In both figures, a filter change at about 8.2  $\mu\text{m}$  can also clearly be seen.

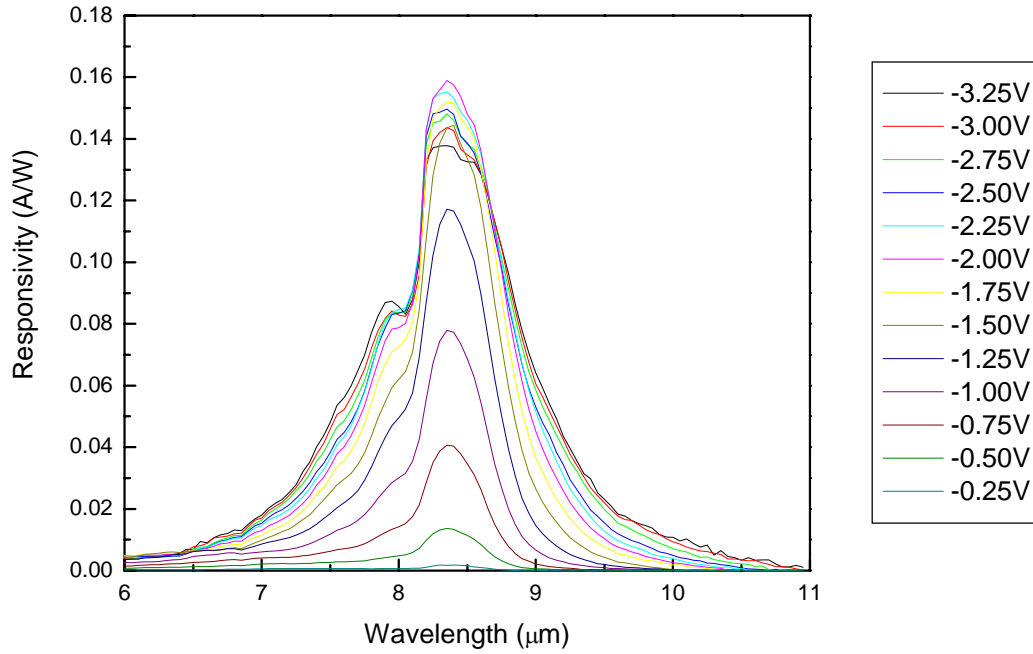


Figure 31. Responsivity as a function of wavelength for the LWIR detector for a set of reverse bias voltages.

### C. TEMPERATURE DEPENDENCE

As discussed earlier, quantum well infrared photodetectors must be operated under cooled conditions to reduce the effect of thermionic emissions. In the I-V measurement portion of this text, the temperature effects on background leakage current were identified and explained. We will now analyze the temperature effects on each device with incident radiation applied.

As temperature increases, electrons within the well are excited to higher energy states. If the thermal energy is large enough, these electrons can contribute to the overall leakage current of the device. In addition to contributing to leakage current, temperature can assist to liberate the photoexcited electrons to a bound state in the well. As a result, additional photocurrent can be expected with increased temperatures. This should ultimately increase the responsivity values.

The temperature dependence measurement for each detector was conducted under constant bias. The 10 K temperature measurements were omitted in this section, because this temperature has already been examined in detail in the previous section.

## 1. Near Infrared Detector

For the temperature dependent spectra shown in Figures 32 and 33, a constant  $\pm 2$  volt bias was applied across the NIR detector for positive and negative biasing, respectively. The wavelength of incident radiation was then changed over a  $0.75\ \mu\text{m}$  to  $1.05\ \mu\text{m}$  range, and photocurrent was recorded at  $0.005\ \mu\text{m}$  steps. Once again, the slit width was reduced to  $0.5\ \text{mm}$  to reduce the incident power on the NIR detector. The average reference detector background voltage was approximately  $4.5\ \text{mV}$ , and no detectable background current was measured for the test detector.

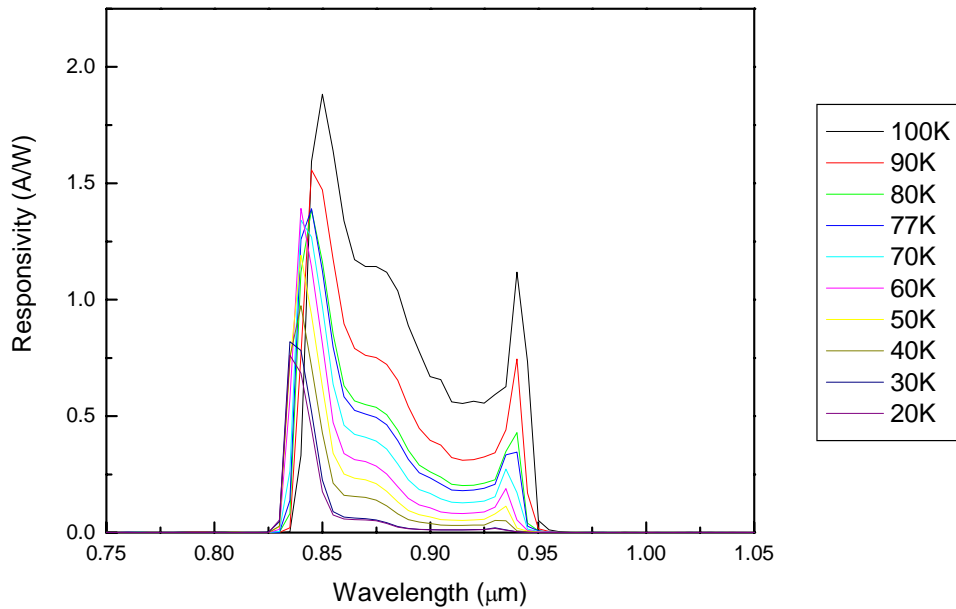


Figure 32. Responsivity as a function of temperature for the NIR detector with a constant 2 V forward bias applied.

In both cases, responsivity increased with temperature mainly due to thermal assisted photocurrent. The slight red shift of the spectra is due to the reduction in bandgap

energy with increasing temperature. The peak responsivity was found to be about 2 A/W at 100 K.

The temperature dependence in forward and reverse bias for the NIR detector was almost identical, with the exception of a slightly higher responsivity for reverse bias measurements. In these figures, three distinct electron transition wavelengths can be observed.

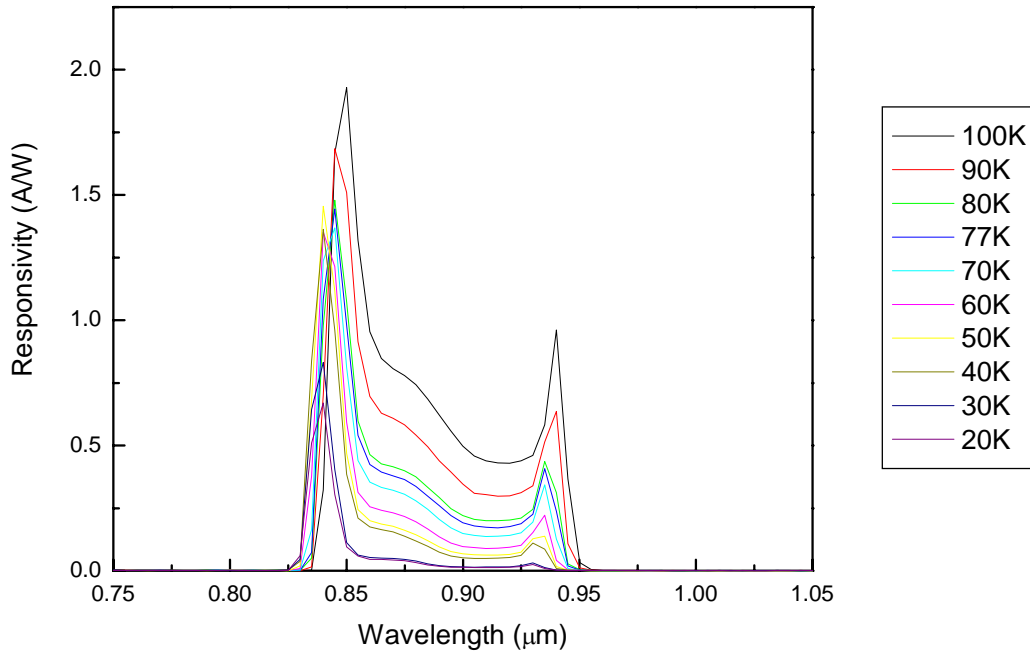


Figure 33. Responsivity as a function of temperature for the NIR detector with a constant -2 V reverse bias applied.

One major difference seen in the temperature dependent curves compared to those of bias dependence is the increase of responsivity monotonically. The electrons undergoing interband transitions are excited to the conduction band and are trapped within the potential well. Due to the additional thermal energy present with increased temperature, electrons are able to transition out of the well and contribute to the detected photocurrent. At low temperatures, this transition is relatively weak. In order to examine this effect more closely, the peak responsivity for the 0.84  $\mu\text{m}$  and 0.93  $\mu\text{m}$  transitions were plotted as a function of temperature in Figure 34. As we can see, the peak

responsivity increases rapidly with temperature. The more significant of the two findings being the unexpected responsivity increase, at 0.93  $\mu\text{m}$  wavelength, with temperature. According to Figure 11, this transition is between the ground states of holes and electrons, where the excited electrons and holes are weakly bounded in the shallow quantum wells. As the temperature is increased the excited electrons and holes can easily be ejected from the respective quantum wells, which increases the photocurrent and hence the responsivity. The effect is not as pronounced for the peak at 0.845  $\mu\text{m}$  since the transition occurs between states close to the barrier.

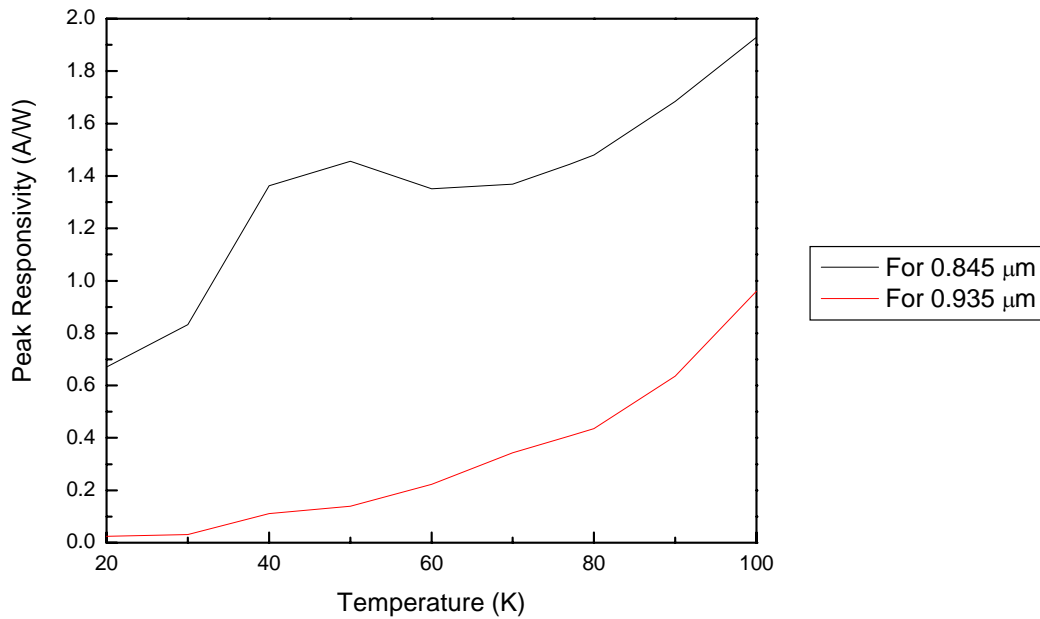


Figure 34. NIR peak responsivity vs. temperature at 0.845  $\mu\text{m}$  and 0.935  $\mu\text{m}$  peaks.

## 2. Mid-Wavelength Infrared Detector

The MWIR temperature dependence was observed over a 4  $\mu\text{m}$  to 6  $\mu\text{m}$  range by plotting photocurrent measurement values at 0.025  $\mu\text{m}$  steps. Each scan was conducted with a constant  $\pm 3.5$  volts, for positive and negative biasing, respectively. The average reference detector background voltage was approximately 6 mV, and the test detector background current was around 0.01 nA. This background current showed slight

variation with temperature. For the MWIR detector, photoexcitation occurs between quantized states in the quantum well formed in the conduction band (as seen in Section I).

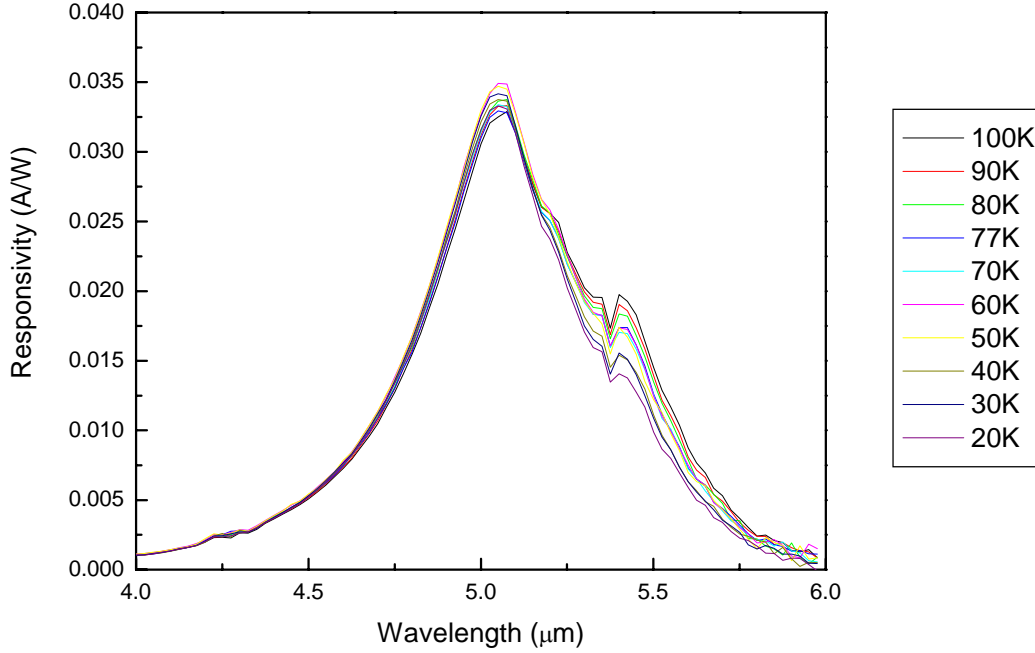


Figure 35. Responsivity as a function of temperature for the MWIR detector with a constant 3.5 V forward bias applied.

Figure 35 and Figure 36 show that there are only very little variations in responsivity with an increase in temperature for the MWIR detector. This is mainly due to a relatively large barrier height that electrons need to climb before escaping, caused by a large separation between the two states in the conduction band needed for MWIR detection. There is very little difference in forward and reverse biasing, with only a slight increase in responsivity being observed in the reverse bias measurements.



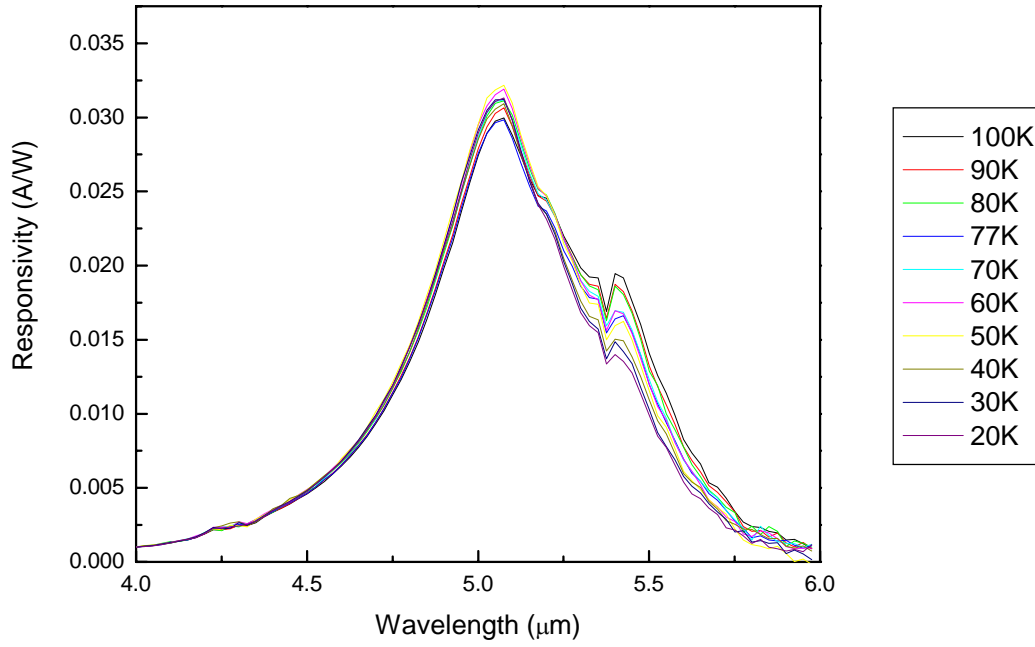


Figure 36. Responsivity as a function of temperature for the MWIR detector with a constant -3.5 V reverse bias applied.

### 3. Long-Wavelength Infrared Detector

The LWIR temperature dependence measurements were taken over a wavelength range of 6 μm to 11 μm in 0.05 μm steps. Due to large leakage current in LWIR detector at high bias, the applied bias was limited to  $\pm 1$  volt. In addition, measurements above 80K were omitted due to a decrease in the signal-to-noise ratio making the measurement unreliable.

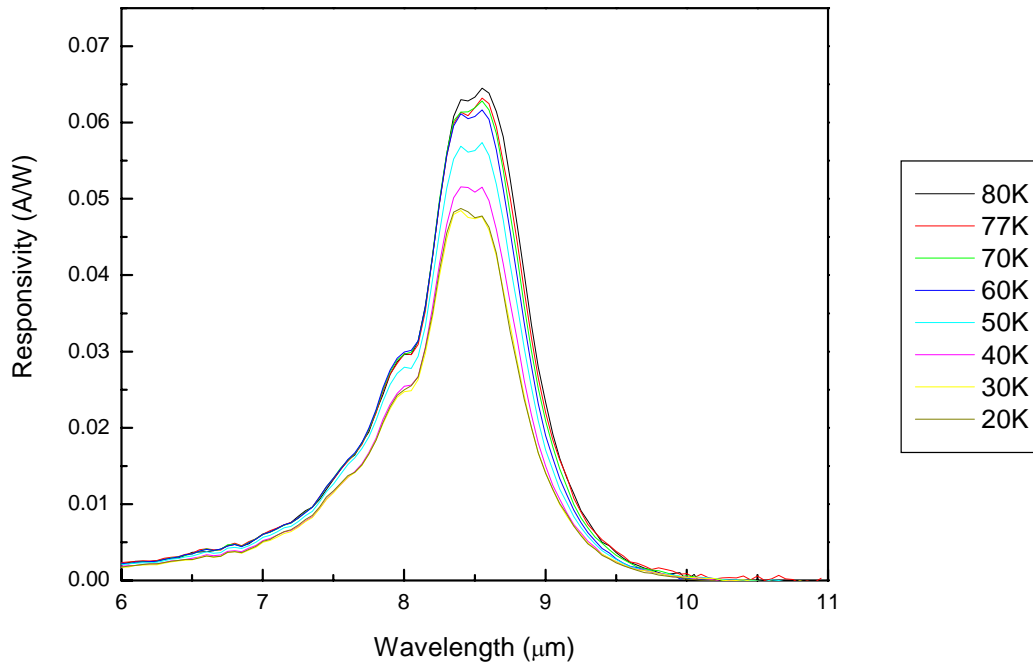


Figure 37. Responsivity as a function of temperature for the LWIR detector with a constant 1 V forward bias applied.

The reference detector average background voltage was approximately 6 mV, and the test detector background current was found to be approximately 0.025 nA. Due to the relatively small bias applied, the peak responsivity seen in Figures 37 and 38 are an order of magnitude lower than the peak responsivities seen previously at higher bias. An increase in peak responsivity can be seen with an increase in temperature, but saturation effects become apparent at high temperatures. There is some spectral response broadening, particularly in the forward bias temperature measurement, but this broadening is relatively minimal.

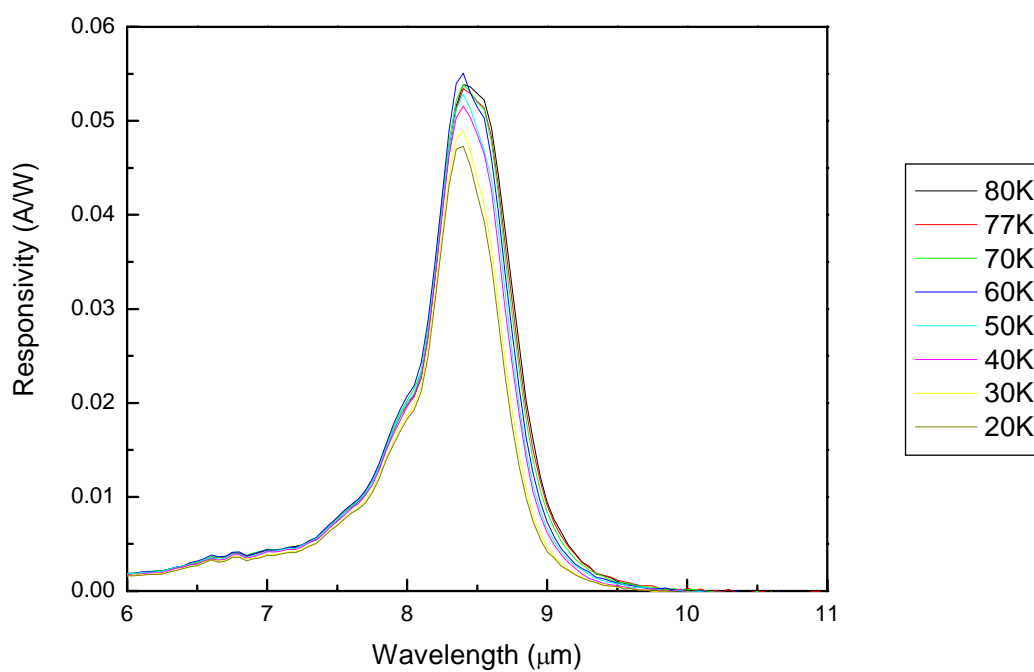


Figure 38. Responsivity as a function of temperature for the LWIR detector with a constant -1 V reverse bias applied.

## **IV. CONCLUSION**

Using quantum well technology as an infrared detection mechanism is not a new concept. In fact, the results of the first quantum well infrared photodetector were published by B. F. Levine in 1987 [10]. However, utilizing these results in conjunction with advancements in fabrication technology and growth processes has enabled much more sophisticated devices to be manufactured. Given the current needs of the U.S. Armed Forces, and future ideals of detection superiority over its enemies, a multicolor QWIP shows prominent signs of enabling us to meet detection and classification objectives.

### **A. OVERALL DETECTOR RELIABILITY**

With the use of photocurrent spectroscopy measurements and dark current analysis, this multicolor quantum well detector has been proven to be highly accurate and sensitive to within design specifications. The peak responsivity outputs in each of these detectors is comparable to those found in QWIP's used to today. The reduced amounts of leakage current measured while operating under normal conditions show that this device can be operated with great sensitivity. An array of these three-mesa structures can be used in cameras or other detection devices with the aid of external computational software. In this way, targets can be identified and classified with much higher accuracy than typical infrared detection devices. The absorption wavelengths found were almost identical to those in the initial design, with only minor deviations irrelevant to initial spectral range criteria. Each device operates well within spectral range limits given by atmospheric absorption and target wavelength range criteria.

Based on the photocurrent and I-V measurements made, optimal operating conditions for each device were found. The undoped NIR detector showed the least amount of dark current present, and was not limited by operating temperature. There was a peak responsivity of 1.3 A/W with -2.25 V reverse bias applied at 0.84  $\mu\text{m}$ . This device

showed three distinct transition wavelength absorption ranges, with high temperature dependence occurring for the 0.93  $\mu\text{m}$  transition in particular. In addition, a cutoff of responsivity could also be seen at about 0.83  $\mu\text{m}$  due to absorption by the substrate. As a result, the optimum operating value for this detector is under a reverse external bias of approximately -2.25 volts.

The doped MWIR detector I-V measurements showed a BLIP at around 80 K except at high ( $\pm 4.5$  V) bias. The peak responsivity for this device was recorded at 5.05  $\mu\text{m}$  rather than the 4.9  $\mu\text{m}$  in its design. This difference is probably due to approximations made in barrier height or slight fabrication uncertainties. The amplitude of responsivity measured is at least an order of magnitude smaller than the NIR device and a factor of four smaller than the LWIR measurements, due to a combination of low doping concentrations and high excitation energy requirements. The well width also had an effect on doping concentration and total responsivity measured. This detector showed a much higher responsivity dependence on external bias, with no significant change in temperature. There was also no significant change in responsivity between forward and reverse bias measurements. As a result, this detector should be operated under a high bias of about 3.5 volts.

The LWIR detector doping concentration was reduced in order to minimize the amount of dark current measured. However, the effects of small barrier heights still limit the operating temperature of this device. Since all three detectors are connected, the LWIR stack will determine the operating temperature limitations for the entire detector. The I-V measurements taken showed a BLIP of approximately 70 K. This limitation rules out liquid nitrogen as a cooling source. In addition, low biases need to be used to ensure saturation conditions do not occur. For the purpose of this analysis, the bias voltage for this device was limited to  $\pm 1$  volt. Even at this low bias, a peak responsivity of 0.065 A/W was measured with 8.4  $\mu\text{m}$  wavelength incident radiation applied.

## **B. MILITARY APPLICATIONS**

Both photodiodes and quantum well infrared detectors can offer multicolor detection capabilities in the MWIR and LWIR regions [1]. However, multicolor detection from the NIR to the LWIR is more likely to be obtained using QWIP's. In an effort to modernize current detection capabilities, the Sensors Research Lab at the Naval Postgraduate School has focused a great deal of attention toward simultaneous, multi-spectral detection techniques. In past research efforts, two-color detection QWIP's have been developed [16]. Now, a new proof-of-concept three-color detection system has been verified to operate in NIR, MWIR and LWIR regions simultaneously. These detectors can be used to enhance military capabilities.

The ability to identify targets using IR signatures has become a crucial factor in military mission success. The use of infrared guided weapons and IR countermeasures has increased demand for a highly sensitive and selective detection device [1]. Currently, extensive focal plane arrays are used to combat this problem. However, these devices are expensive, complex, and have extensive power and cooling requirements. With new computational software techniques and further analysis of operational limitations, multi-color quantum well infrared photodetectors may prove to be the logical progression in staying ahead in the realm of detection techniques.

## **C. RECOMMENDATIONS AND FUTURE WORK**

The multicolor quantum well infrared detector described in this thesis showed absorption and response characteristics expected with its design. Detection in the NIR, MWIR, and LWIR ranges were achieved within operational limits. Future areas of study may include more advanced simulation techniques, the use of different material layers, and analysis of fabrication variation effects on device performance. The use of gratings and better fabrication methods may prove useful to create more sensitive and shorter

spectral range devices. Ultimately, this device will have to be implemented into a camera or other detection device in order to make it operational. This may be the work for future research projects.

## **APPENDIX A: AGILENT 4155B SEMICONDUCTOR PARAMETER ANALYZER OPERATION**

In order to take I-V measurements using the Agilent 4155B Semiconductor Parameter Analyzer, you will need to:

- 1.) Connect biasing leads across the device.
- 2.) Select the MEM4 (Diode) button on the bottom left of the console.
- 3.) Push the “Measure” key.
- 4.) Select LIN/LG (Linear).
- 5.) Enter Start, End, Step, and Compliance values to scan.

Example:

Start: -1.0 V

End: 1.0 V

Step: 10.0 mV

Compliance: 1.0 mA

- 6.) Use display button to adjust display ranges.
- 7.) To sweep: push “Single” button on top right of console.
- 8.) To save: (Note: all letters must be in CAPS, you will need a 3.5” floppy disk)

Push “Graph/List” button

Select “spreadsheet”

Push “All”

Hit “Execute” button



THIS PAGE INTENTIONALLY LEFT BLANK

## LIST OF REFERENCES

- [1] Alves, Fabio D. P., "Design and Analysis of a Multicolor Quantum Well Infrared Photodetector," Master's Thesis, Naval Postgraduate School, Monterey, CA, September 2005.
- [2] Coon, D. D. and G. Karunasiri, "New Mode of IR Detection Using Quantum Wells," *Applied Physics Letters*, Vol. 45, pp. 649-652, 1984.
- [3] Dereniak, E. L. and G. D. Boreman, *Infrared Detectors and Systems*, John Wiley & Sons, Inc., 1996.
- [4] Harwit, A. and J. S. Harris, "Observations of Stark Shifts in Quantum Well Intersubband Transitions," *Applied Physics Letters*, Vol. 50, pp. 685, 1987.
- [5] Herdlick, Bryan E., "Computer-Controlled Photodetector Characterization System (Design and Construction)," Master's Thesis, Naval Postgraduate School, Monterey, CA, December 2002.
- [6] Hickey, Thomas R., "Temperature Dependence of Dark Current in Quantum Well Infrared Photodetectors," Master's Thesis, Naval Postgraduate School, Monterey, CA, June 2002.
- [7] Hudson, R., *Infrared System Engineering*, John Wiley & Sons, Inc., 1969.
- [8] Karunasiri, G., Notes for PH-4272 (Lasers, Optoelectronics & Electro-Optics II), Naval Postgraduate School, June 2006 (unpublished).
- [9] Keng, Lim Poh, "Computerized Measurement of the Photoresponse of Infrared Photodetectors," National University of Singapore.
- [10] Levine, B. F., K. K. Choi, C. G. Bethea, J. Walker and R. J. Malik "New 10  $\mu\text{m}$  Infrared Detector Using Intersubband Absorption in Resonant Tunneling GaAlAs Superlattices," *Applied Physics Letters*, Vol. 50, No. 16, pp. 1092-1094, 1987.

[11] Levine, B. F., “Quantum Well Infrared Photodetectors,” *Journal of Applied Physics*, Vol. 74, No. 8, pp. 1-72, 1993.

[12] Liboff, Richard L., *Introductory Quantum Mechanics*, Fourth Ed., Addison Wesley, San Francisco, 2003.

[13] Rogalski, A., K. Adamiec, and J. Rutkowski, *Narrow-Gap Semiconductor Photodiodes*, SPIE Press, 2000.

[14] Shubert, E. F., Notes for ECSE-6968 (Quantum Mechanics Applied to Semiconductor Devices), Rensselaer Polytechnic Institute, October, 2004 (unpublished).

[15] Tiong, Yeo Hwee, “High Responsivity Tunable Step Quantum Well Infrared Photodetector,” Master’s Thesis, Naval Postgraduate School, Monterey, CA, December 2004.

[16] Touse, Michael P., “Demonstration of a Near and Mid-Infrared Detector Using Multiple Step Quantum Wells,” Master’s Thesis, Naval Postgraduate School, Monterey, CA, September 2003.

## **INITIAL DISTRIBUTION LIST**

1. Defense Technical Information Center  
Ft. Belvoir, Virginia
2. Dudley Knox Library  
Naval Postgraduate School  
Monterey, California
3. Prof. Gamani Karunasiri  
Naval Postgraduate School  
Monterey, California
4. Prof. James H. Luscombe  
Naval Postgraduate School  
Monterey, California